# Tubulin CFEOM mutations both inhibit or activate kinesin motor activity

Anna Luchniak<sup>a,†</sup>, Pallavi Sinha Roy<sup>a,†</sup>, Ambuj Kumar<sup>b</sup>, Ian C. Schneider<sup>a,c</sup>, Vladimir I. Gelfand<sup>d</sup>, Robert L. Jernigan<sup>b</sup>, and Mohan L. Gupta, Jr.<sup>©</sup>, and Mohan L. Gupta, Jr.<sup>©</sup>

<sup>a</sup>Genetics, Development and Cell Biology, <sup>b</sup>Bioinformatics and Computational Biology Program, Roy J. Carver Department of Biochemistry, Biophysics and Molecular Biology, and <sup>c</sup>Department of Chemical and Biological Engineering, Iowa State University, Ames, IA 50011; <sup>d</sup>Cell and Developmental Biology, Feinberg School of Medicine, Northwestern University, Chicago, IL, 60611

ABSTRACT Kinesin-mediated transport along microtubules is critical for axon development and health. Mutations in the kinesin Kif21a, or the microtubule subunit β-tubulin, inhibit axon growth and/or maintenance resulting in the eye-movement disorder congenital fibrosis of the extraocular muscles (CFEOM). While most examined CFEOM-causing β-tubulin mutations inhibit kinesin-microtubule interactions, Kif21a mutations activate the motor protein. These contrasting observations have led to opposed models of inhibited or hyperactive Kif21a in CFEOM. We show that, contrary to other CFEOM-causing β-tubulin mutations, R380C enhances kinesin activity. Expression of \( \beta\)-tubulin-R380C increases kinesin-mediated peroxisome transport in S2 cells. The binding frequency, percent motile engagements, run length and plus-end dwell time of Kif21a are also elevated on  $\beta$ -tubulin-R380C compared with wildtype microtubules in vitro. This conserved effect persists across tubulins from multiple species and kinesins from different families. The enhanced activity is independent of tail-mediated kinesin autoinhibition and thus utilizes a mechanism distinct from CFEOM-causing Kif21a mutations. Using molecular dynamics, we visualize how β-tubulin-R380C allosterically alters critical structural elements within the kinesin motor domain, suggesting a basis for the enhanced motility. These findings resolve the disparate models and confirm that inhibited or increased kinesin activity can both contribute to CFEOM. They also demonstrate the microtubule's role in regulating kinesins and highlight the importance of balanced transport for cellular and organismal health.

Monitoring Editor Claire Walczak Indiana University

Received: Jan 23, 2023 Revised: Dec 12, 2023 Accepted: Dec 19, 2023

### SIGNIFICANCE STATEMENT

- Neurons require axonal transport by kinesin motor proteins along microtubules. Kinesin mutations
  that increase, or tubulin mutations that decrease transport cause the eye-movement disorder, congenital fibrosis of the extraocular muscles (CFEOM).
- Whether enhanced or diminished transport promotes CFEOM remains uncertain. Using in vitro reconstitution, vesicle transport in Drosophila S2 cells, and molecular dynamics modeling, the authors
  show a subset of CFEOM-causing tubulin mutations allosterically enhance kinesin activity.
- These findings resolve the opposed models by revealing tubulin mutations increasing or decreasing transport contribute to similar CFEOM. They also suggest the microtubule plays an essential role in regulating kinesin function.

This article was published online ahead of print in MBoC in Press (http://www.molbiolcell.org/cgi/doi/10.1091/mbc.E23-01-0020) on January 3, 2024.

Conflict of Interest: The authors declare no competing interests.

†These authors contributed equally.

Author Contributions: A.L, P.SR., A.K., I.C.S., V.I.G., R.L.J., and M.L.G. analyzed and interpreted results; A.L., P.SR., A.K., and M.L.G. performed experiments, analyzed data, prepared figures, and wrote the manuscript. All authors participated in editing the manuscript.

\*Address correspondence to: Mohan L. Gupta, Jr. (mgupta@iastate.edu). Abbreviations used: ADP, adenosine diphosphate; ALS, amyotrophic lateral sclerosis; AMP-PNP, 5'-adenylylimidodiphosphate; ATP, adenosine triphosphate; CFEOM, congenital fibrosis of the extraocular muscles; CFP, cyan fluorescent

protein; ConA, concanavalin A; DCX, doublecortin; GDP, guanosine diphosphate; GFP, green fluorescent protein; GMPCPP, guanosine-5'-[( $\alpha$ , $\beta$ )-methyleno]triphosphate; GTP, guanosine triphosphate; HSP, hereditary spastic paraplegia; K-S test, Kolmogorov-Smirnov test; MAP, microtubule-associated protein; MD, molecular dynamics; NOLB, nonlinear rigid block normal-mode analysis; RMSF, root-mean-square fluctuation; SD, standard deviation; SEM, standard error of the mean; TIRF, total internal reflection fluorescence; YFP, yellow fluorescent protein.

© 2024 Luchniak et al. This article is distributed by The American Society for Cell Biology under license from the author(s). Two months after publication it is available to the public under an Attribution–Noncommercial–Share Alike 4.0 Unported Creative Commons License (http://creativecommons.org/licenses/by-nc-sa/4.0). "ASCB®," "The American Society for Cell Biology®," and "Molecular Biology of

the Cell®" are registered trademarks of The American Society for Cell Biology.

#### INTRODUCTION

Intracellular transport involves translocation of materials by molecular motor proteins along microtubules and is essential for a range of cellular functions (Kapitein and Hoogenraad, 2015; Barlan and Gelfand, 2017). It is particularly important for nervous system development and health, which requires the delivery of materials over long distances where diffusion would be ineffective (Kapitein and Hoogenraad, 2015; Mogre et al., 2020). Microtubule-dependent transport is also critical for the development and long-term maintenance of axons (Guillaud et al., 2020). A growing number of mutations in the protein subunit of microtubules, tubulin, and in the microtubule-dependent motor proteins, kinesin, have been shown to cause human neurological disorders (Bahi-Buisson et al., 2014; Kalantari and Filges, 2020; Jurgens et al., 2021).

Anterograde transport in axons is carried out by kinesin motor proteins traveling along microtubules. A critical aspect of long-distance intracellular transport is the ability of kinesin to take multiple processive steps along the microtubule without dissociating (Hancock, 2016). Microtubules are cylindrical filaments that assemble from tubulin, which is a heterodimer of  $\alpha$ - and  $\beta$ -subunits (Nogales, 2000). Because tubulin assembles in a head-to-tail manner, the resulting microtubule is polar with  $\alpha$ - and  $\beta$ -tubulin subunits positioned at the "minus" and "plus" ends, respectively. Within axons, microtubules form organized arrays with uniform polarity, which facilitates anterograde and retrograde transport by plus-end directed kinesin and minus-end directed dynein motors, respectively (Kapitein and Hoogenraad, 2015; Guillaud et al., 2020). During processive transport by dimeric kinesin, efficient chemomechanical coupling between the two motor domains ensures that one is always securely bound to the microtubule as they alternately move from the trailing to the leading position and "step" from one underlying tubulin to the next (Hancock, 2016; Gilbert et al., 2018). Thus, processivity is achieved by regulated allosteric changes in the two motor domains that coordinate ATP hydrolysis and microtubule binding.

An expanding number of mutations in tubulin and the kinesin Kif21a are known to cause congenital fibrosis of the extraocular muscles (CFEOM), an eye-movement disorder caused by impaired axon growth and/or maintenance that prevents the oculomotor nerve from properly innervating ocular muscles (Traboulsi and Engle, 2004; Tischfield et al., 2010; Cederquist et al., 2012; Cheng et al., 2014; Ryan and Engle, 2015; Al-Haddad et al., 2020; Jurgens et al., 2021). While mutations in the tubulin isotypes Tubb3, Tubb2b, or Tuba1a often result in CFEOM accompanied with other neurological developmental disorders (Tischfield et al., 2010; Cederquist et al., 2012), those in Kif21a generally cause isolated CFEOM (Yamada et al., 2003). Through efforts to understand the molecular etiology, most CFEOM tubulin mutations that have been examined significantly impair kinesin interaction with, or motility along microtubules (Tischfield et al., 2010; Cederquist et al., 2012; Niwa et al., 2013; Minoura et al., 2016; Ti et al., 2016). Surprisingly, Kif21a CFEOM mutations were subsequently found to enhance kinesin's activity by preventing the normal head-to-tail autoinhibition of the motor (Cheng et al., 2014). This led to the opposed models for CFEOM development; in the first, tubulin mutations diminish kinesin-mediated transport while, in the second, mutations in Kif21a boost kinesin activity. This resulting dichotomy challenges the idea that tubulin and Kif21a mutations both cause CFEOM by perturbing kinesin activity, as one decreases and the other increases activity. It instead raises the possibility that the tubulin mutations may generate the CFEOM phenotype via a fundamentally different mechanism than Kif21a mutations.

We set out to address this paradox by investigating whether similar CFEOM phenotypes arise from tubulin mutations that differentially diminish or enhance kinesin activity. While it is logical that disrupted microtubule-dependent transport would be detrimental to axon health, it is less clear whether enhanced transport would be similarly harmful. We hypothesize that if activity-boosting mutations in Kif21a can cause CFEOM (Cheng et al., 2014), then increasing Kif21a activity by an alternative method would result in a similar phenotype. Here, we find that the  $\beta$ -tubulin-R380C mutation enhances multiple parameters of kinesin-dependent transport both in vitro and in vivo. This increase occurs via a fundamentally different mechanism than that observed in CFEOM-causing Kif21a mutations. We also directly confirm that the D417H mutation disrupts kinesin function. Using molecular modeling we reveal how R380C allosterically impacts the structural elements in kinesin that mediate processive motility. Our results unify the apparently disparate models for how mutations in tubulin or kinesin result in CFEOM by showing that different tubulin mutations, which result in similar phenotypic outcomes, either inhibit or enhance kinesin activity. They also highlight the role of the microtubule track in regulating the molecular motions of kinesin needed for processive motility.

### **RESULTS**

# $\beta$ -tubulin-R380C increases kinesin binding and productive engagement on microtubules

The CFEOM tubulin mutations examined to date support a mechanism of disrupted kinesin interaction with the mutant-containing microtubules (Tischfield et al., 2010; Cederquist et al., 2012; Niwa et al., 2013; Minoura et al., 2016). Strikingly, and opposite to those CFEOM tubulin mutations, the  $\beta$ -tubulin R380C substitution significantly enhances microtubule localization of the kinesin Kip3 in yeast cells (Figure 1A; Tischfield et al., 2010). This prompted us to examine whether the  $\beta$ -tubulin R380C mutation may function to enhance kinesin activity.

To quantify kinesin activity in vitro we established a total internal reflection fluorescence (TIRF) microscopy-based assay (Supplemental Figure S1A). Microtubules were assembled from purified wildtype and  $\beta$ -R380C yeast tubulin (Supplemental Figure S1B). Another β-tubulin mutation, D417H, was utilized as a representative CFEOM mutation that disrupts kinesin interaction (Figure 1A). Mouse Kif21a, which is highly conserved with human Kif21a (Supplemental Figure S1F), fused to GFP was expressed in HEK293T cells and dilute, clarified extracts were applied to flow chambers containing GMPCPPstabilized microtubules (Cheng et al., 2014). Photobleaching analysis demonstrated our assay monitors dimeric Kif21a-GFP and not higher order clusters and/or aggregates functioning together (Supplemental Figure S1, C-E). Kinesin interaction and motility on microtubules was quantified from kymographs (Figure 1B). Compared to wildtype microtubules, we found that R380C produces a 29% increase in Kif21a binding frequency (Figure 1E). Moreover, more than twice the number of binding events detected on R380C microtubules result in productive motility (Figure 1E). By contrast, the D417H mutation severely diminishes overall binding and motility events (Figure 1E).

Several classes of kinesins are autoinhibited by intramolecular interactions between the motor domain and distal regions of the extended stalk and tail (Figure 1C; Coy et al., 1999; Friedman and Vale, 1999; Stock et al., 1999). A subset of Kif21a CFEOM mutations are known to disrupt the autoinhibitory interaction between the motor domain and the third coiled-coil region of the stalk

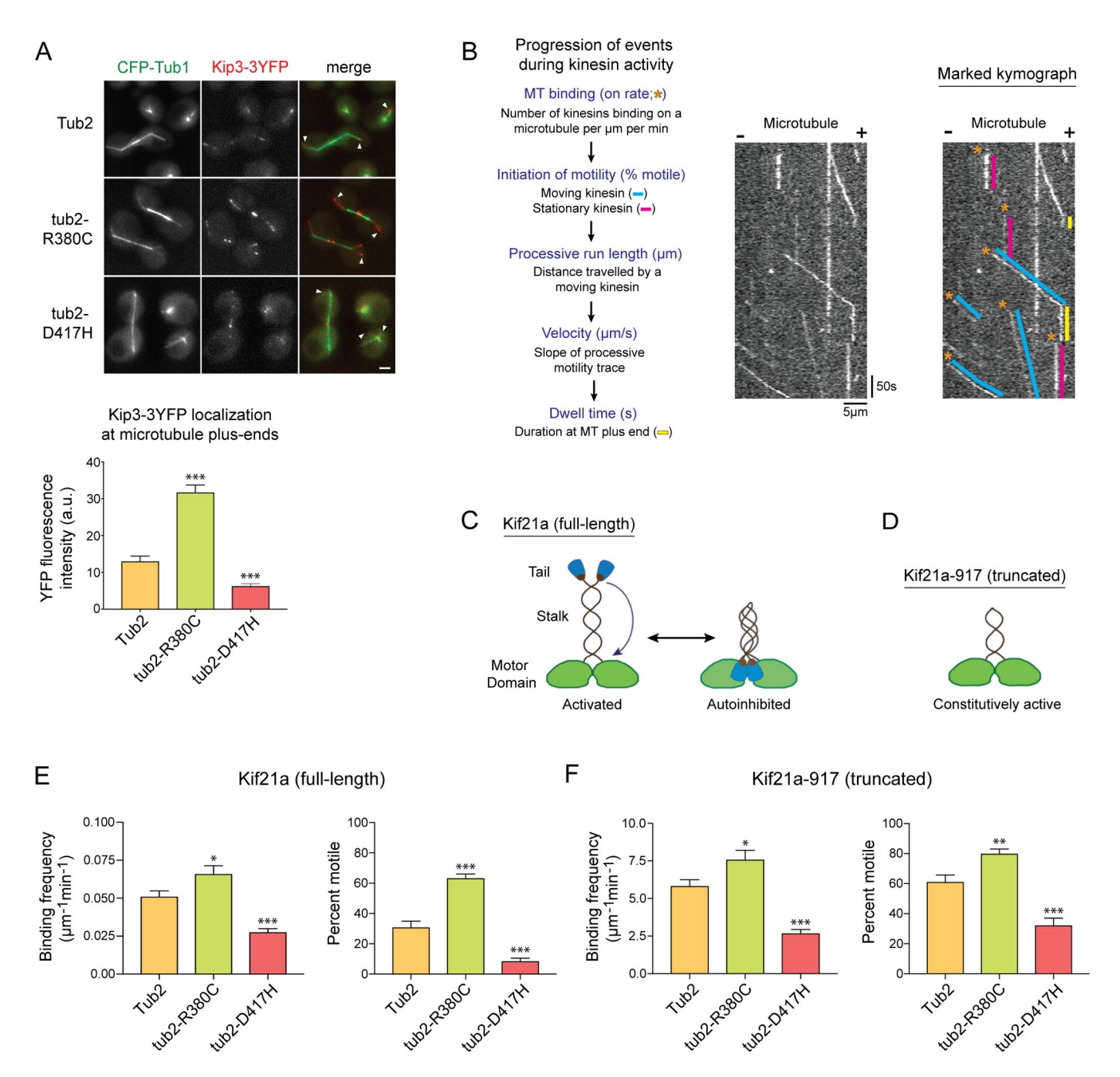


FIGURE 1: β-tubulin-R380C increases kinesin binding and productive engagement on microtubules. (A) Top: maximum projected Z-stack images of Kip3-3YFP (red) on wildtype and mutant microtubules labeled with CFP-Tub1 (α-tubulin, green) in yeast cells. White arrowheads denote representative astral microtubule plus-ends. Signal intensity adjusted equally in all images for comparison. Bottom: graph shows mean Kip3-3YFP levels at astral microtubule plus-ends. Scale bar = 2 µm. (B) Events during kinesin-microtubule interaction (left) and representative kymograph of Kif21a-GFP activity on a microtubule in vitro monitored by TIRF microscopy (center). Representative kinesin events are indicated by asterisks and colors on the marked kymograph (right). (C and D) Head-to-tail interaction autoinhibits full-length Kif21a (C) but not the truncated Kif21a-917 (D). (E and F) Binding frequency and percent of binding events that result in processive motility for (E) Kif21a and (F) truncated Kif21a-917. In (A) n = 202 plus-ends from two independent clones on two independent days for each genotype. For (E) n = 353, 310, and 179 from 31, 28, and 31 microtubules, for (F) n = 302, 375, and 123 from 26, 30, and 30 microtubules for Tub2, Tub2-R380C, and Tub2-D417H, respectively. For all panels graphs depict mean  $\pm$  SEM; asterisks denote p values compared with Tub2; \*  $p \le 0.05$ , \*\*  $p \le 0.01$ , and \*\*\*  $p \le 0.001$  by unpaired Student's t test. See also Supplemental Figure S1.

(Cheng et al., 2014; Bianchi et al., 2016). This autoinhibition can be constitutively removed by truncation at position 917 before the third coiled-coil, referred to as Kif21a-917 (Figure 1D; Supplemental Figure S1G; Cheng et al., 2014).

To gain insight into the mechanism by which R380C tubulin increases kinesin activity we tested kif21a-917 in our TIRF assay. We reasoned that if R380C functions to antagonize autoinhibition of Kif21a, then removal of the distal stalk and tail in Kif21a-917, which precludes autoinhibition, should eliminate the increased activity on R380C compared with wildtype microtubules. As expected, binding of Kif21a-917 to wildtype microtubules is increased ~100-fold relative to full-length Kif21a (compare Figure 1, E and F). Strikingly, despite this 100-fold increase, the binding frequency of Kif21a-917 is further elevated another 31% on R380C over wildtype microtubules (Figure 1F).

Whereas only ~30% of full-length Kif21a binding events result in productive motility on wildtype microtubules, that percentage is doubled to 61% for Kif21a-917, as expected for an uninhibited motor (compare Figure 1, E and F). On R380C microtubules, the percentage of Kif21a-917 binding events that result in productive motility is further increased by 30% (Figure 1F). Opposite to the effect of R380C, the D417H mutation severely inhibits both the overall binding as well as the initiation of productive motility following Kif21a-917 binding to the microtubule (Figure 1F).

Considering the binding rate and the percentage of those events that result in processive motility, at identical Kif21a concentrations, nearly three times as many productive interactions occur on R380C compared with wildtype microtubules (0.042  $\pm$  0.004 vs. 0.016  $\pm$  0.002  $\mu m^{-1} min^{-1}$ , mean  $\pm$  SEM, respectively). For the constitutively active Kif21a-917, the number of productive interactions on R380C remains almost twice as high as that on wildtype microtubules (6.06  $\pm$  0.02 vs. 3.56  $\pm$  0.02  $\mu m^{-1} min^{-1}$ , mean  $\pm$  SEM, respectively). In contrast, both full-length and truncated Kif21a display significantly fewer productive interactions on D417H relative to wildtype microtubules (Figure 1, E and F).

These results demonstrate that the R380C mutation increases the binding frequency as well as the fraction of encounters that result in productive motility of Kif21a along the microtubule. A similar level of activation occurs with Kif21a-917, which does not undergo the known head-to-tail autoinhibition (Cheng et al., 2014; Bianchi et al., 2016). Thus, the effect of R380C is independent of this Kif21a autoinhibition mechanism.

# $\beta$ -tubulin-R380C increases the processive run length of Kif21a

We next asked whether the tubulin R380C mutation affects other parameters of kinesin function. Following productive binding Kif21a undergoes processive plus-end-directed motility along the microtubule. During this process, chemomechanical coupling between the two motor domains ensures at least one is securely bound to the microtubule while they alternately advance from the trailing to the leading position. In this way kinesin can take many processive "steps" toward the plus-end before disengaging the microtubule.

For both Kif21a and the truncated Kif21a-917, individual run lengths form lognormal distributions. For full-length Kif21a on wildtype microtubules, the "geomean" of the distribution, or midpoint at which half the runs are longer, and half shorter, is 0.68 µm. The "center" of the distribution, or run length with the highest frequency is 0.29 µm (Figure 2A). The distribution of Kif21a run lengths on R380C microtubules is significantly skewed toward longer distances (p = 0.039 by K–S test; Figure 2A). Although the geomean of run lengths is only slightly elevated, the center of the distribution is 61% higher than on wildtype microtubules with distinct 95% confidence intervals (0.27–0.30 vs. 0.45–0.48  $\mu m$  for wildtype and R380C, respectively; Figure 2A). This reveals that R380C enhances run length, and with full-length Kif21a the effect may be observed predominantly on shorter runs. Compared to wildtype, run lengths on D417H microtubules are significantly reduced (p = 0.0043 by K–S test; Figure 2A). The geomean and center are both reduced ~30% (95% confidence interval 0.16-0.23 vs. 0.27-0.30 for D417H and wildtype, respectively).

Consistent with the lack of autoinhibition, run lengths of the truncated Kif21a-917 are significantly increased compared with full-length Kif21a. On wildtype microtubules Kif21a-917 runs display a geomean of 4.03  $\mu m$  and center of 1.56  $\mu m$ , compared with 0.68 and 0.29, respectively, for full-length Kif21a (Figure 2; Supplemental Figure S2A). The distribution of Kif21a-917 run lengths is significantly altered on R380C and D417H microtubules (p=0.041 and <0.0001 by K–S test for wildtype vs. R380C and D417H, respectively). The center of the run lengths is increased 13% on R380C and decreased 68% on D417H microtubules (Supplemental Figure S2A).

When the ionic strength of the buffer is increased by addition of 100 mM KCI, the geomean and center of Kif21a-917 run lengths on wildtype microtubules is somewhat decreased to 1.74 and 0.63  $\mu$ m, respectively (Figure 2B). Under these more stringent binding conditions, however, the effect of R380C on run length distribution is even more apparent (p=0.004 by K–S test). Compared to wildtype, the geomean is increased 30% and the center is 56% higher (Figure 2B; 95% CI for center = 0.54–0.71 vs. 0.90–1.05  $\mu$ m for wildtype and R380C, respectively). Compared to wildtype, the distribution is shifted toward shorter run lengths on D417H microtubules (p<0.0001 by K–S test), with both center and geomean reduced by ~45% (Figure 2B).

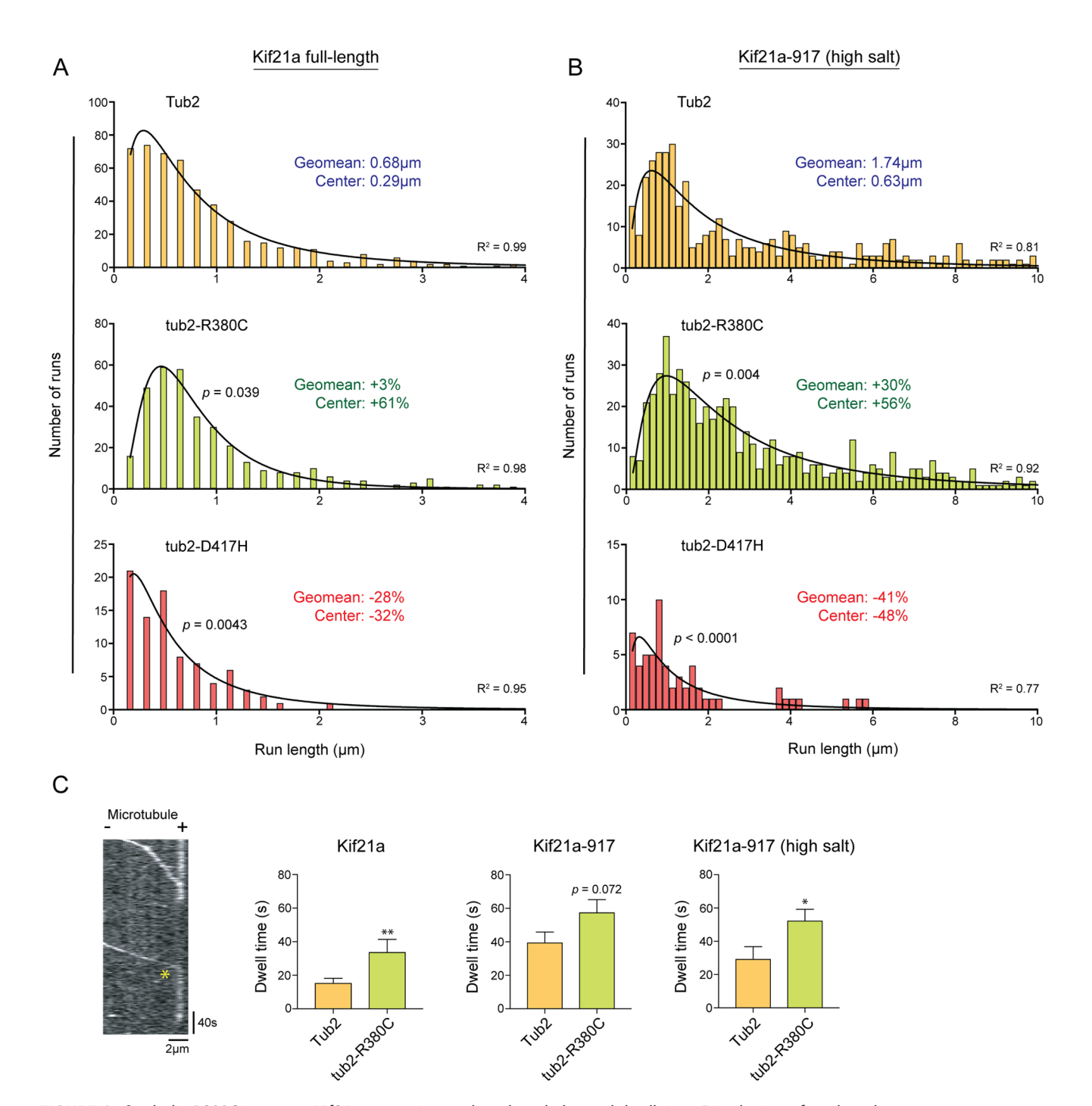
The length distributions of wildtype, R380C and D417 microtubules analyzed in these assays are statistically indistinguishable under all conditions tested, which shows that polymer length is not a limiting factor responsible for the observed changes in run lengths (Supplemental Figure S3). Altogether the results demonstrate that  $\beta$ -tubulin-R380C enhances Kif21a run length. As with productive binding rates, the influence of R380C is opposite to that of D417H, which sharply decreases run length. These effects are also seen with truncated Kif21a-917. Thus, the mechanisms by which R380C and D417H alter run length are independent of the autoinhibition mediated by the distal stalk region.

# $\beta$ -tubulin-R380C does not significantly alter the velocity of Kif21a

We did not observe a statistically significant change in the geomean of velocities on R380C relative to wildtype microtubules with the full-length or truncated Kif21a constructs (Supplemental Figure S2B). The D417H mutation, however, reduces velocity by 30–65% for full-length Kif21a and Kif21a-917 (Supplemental Figure S2B). The reduced velocity on D417H microtubules is statistically significant for Kif21a-917 under both lower and higher ionic strength conditions (p < 0.0001 for both by K–S test). Thus, R380C does not significantly alter Kif21a velocity, whereas the motor is clearly slower on microtubules harboring the D417H mutation.

# β-tubulin-R380C significantly increases the plus-end dwell time of Kif21a

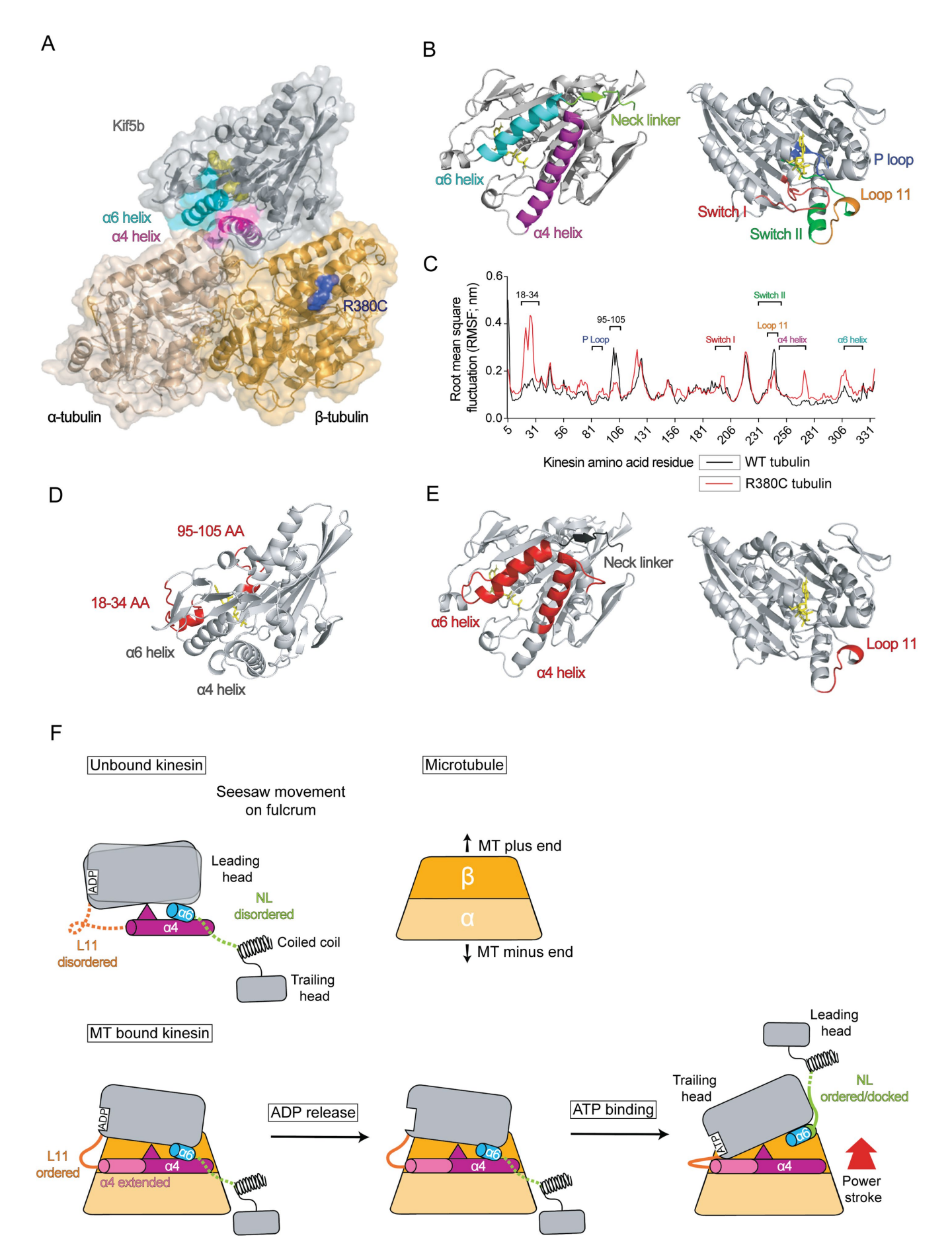
When a kinesin reaches the end of a microtubule it can remain bound, transiently "dwelling" before disengaging. Compared to wildtype, this dwell time is doubled when Kif21a encounters the end of an R380C microtubule (Figure 2C). With truncated Kif21a-917 the dwell time increases by 45% on R380C relative to wildtype microtubules, and is also nearly doubled under the more stringent, high salt binding conditions (Figure 2C). The dwell time on D417H microtubules could not be reliably determined due to the small number of kinesin molecules successfully reaching the end of these polymers. The longer dwell times are consistent with increased binding affinity, and/or more efficient chemomechanical coupling between the kinesin motor domains on R380C microtubules.



 $\textbf{FIGURE 2:} \ \, \beta\text{-tubulin-R380C increases Kif21a processive run length and plus-end dwell time.} \ \, \text{Distribution of run lengths}$ on wildtype and mutant microtubules for (A) full-length Kif21a, and for (B) truncated Kif21a-917 under increased ionic strength conditions. Based on lognormal curve fits, geomean (geometric mean) = median, or characteristic run length, center = run length with highest frequency. (C) Representative kymograph (left) showing Kif21a-GFP "dwell" (yellow asterisk) at microtubule plus-end. Graphs depict dwell times (mean ± SEM). For (A and B) p values shown are calculated based on the comparison with wildtype Tub2 using Kolmogorov-Smirnov test. In (A) n = 514, 348, and 85 from 163, 61, and 86 microtubules over three experiments, and in (B) n = 438, 595, and 60 from 56, 50, and 49 microtubules over two trials for Tub2, Tub2-R380C, and Tub2-D417H, respectively. In (C) for Kif21a n = 61, 40, Kif21a-917 n = 70, 72, and Kif21a-917 (high salt) n = 48, 51 from four experiments for each; \*  $p \le 0.05$ , \*\*  $p \le 0.01$  by unpaired Student's t test. See also Supplemental Figures S2 and S3.

# β-tubulin-R380C allosterically impacts kinesin regions critical for chemomechanical activity and processive motility

Processive kinesin motility requires efficient chemomechanical coupling between the two motor heads. Binding to the microtubule induces allosteric changes in kinesin that coordinate ATP hydrolysis and thus, are essential for processivity (Figure 3, A and B; Sindelar and Downing, 2010; Gigant et al., 2013; Atherton et al., 2014; Shang et al., 2014). The R380C substitution is located away from the



kinesin-microtubule binding interface, on the distal side of the kinesin-binding tubulin helixes  $\alpha 11$  and 12, yet it increases kinesin binding and processivity nonetheless (Figure 3A). We hypothesize that R380C alters the dynamic interaction and allosteric changes induced in kinesin during microtubule binding. To investigate this possibility, we carried out molecular dynamics (MD) simulations and elastic network modeling analyses of kinesin bound to tubulin and the microtubule, respectively.

To increase atomic precision in our default structure we used that obtained from the single isotype Tub1/Tub2 heterodimer determined in microtubules (Howes et al., 2017), which also corresponds to the tubulin utilized for the in vitro assays reported here. There is currently no structure reported for the motor domain of any Kif21a family member. Thus, we utilized the ~5 Å resolution structure of the microtubule-bound, plus-end directed motor Kif5b (Shang et al., 2014), that belongs to the same kinesin-1 family that we show below, in Figure 4, is upregulated by R380C tubulin. The Kif5b structure was docked onto two independently relaxed wildtype tubulin structures and two independently relaxed R380C tubulin structures (Shang et al., 2014). Each of these complexes was further relaxed in two independent MD simulations over another 200 ns, generating four wildtype and four R380C kinesin-docked tubulin structures. These four independently relaxed structures for each tubulin isotype were used to determine the root-mean-square fluctuation (RMSF) for each alpha carbon atom. When kinesin interacts with R380C tubulin, five segments of the motor domain display large RMSF changes relative to those of the motor bound to wildtype tubulin (Figure 3C). While three of these segments are near the microtubule binding surface, another two, amino acid numbers 18-34 and 95-105, are relatively distant from the binding surface and, although 95-105 is adjacent to the P-loop, neither is known to be directly important for kinesin translocation (Figure 3D).

Strikingly, the other three kinesin segments that display altered RMSF play key roles in the chemomechanical cycle and processive motility (Figure 3E). Helix  $\alpha 4$  forms the main microtubule binding structure of kinesin and settles into the groove between the  $\alpha$ - and β-tubulin subunits (Figure 3, A and B). Microtubule binding promotes stabilization of the end of  $\alpha 4$  that leads into the loop 11/ switch II motif (Sindelar and Downing, 2010; Gigant et al., 2013; Atherton et al., 2014; Shang et al., 2014). The microtubule binding state is thus transmitted via conformational changes in loop 11/ switch II to regulate the hydrolysis of ATP (Figure 3B; Sindelar and

Downing, 2010; Gigant et al., 2013; Atherton et al., 2014; Shang et al., 2014). Loop 11, which is a critical component of switch II displays decreased flexibility when the kinesin is bound to the R380C tubulin in comparison with wildtype (Figure 3, C and E). Helix  $\alpha$ 6 links microtubule binding and ATP hydrolysis to the repositioning of the neck linker to thrust the trailing motor head into the leading position (Rice et al., 2003; Sindelar and Downing, 2010; Gigant et al., 2013; Atherton et al., 2014; Shang et al., 2014). This region shows increased flexibility when bound to the R380C tubulin (Figure 3, C and E). Moreover, the end of  $\alpha 4$  that is distant to loop 11/switch II must undergo a conformational change to allow the neck linker, attached to  $\alpha$ 6, to reorient during the stepping motion (Figure 3F; Gigant et al., 2013; Shang et al., 2014). Notably, this region of  $\alpha 4$  experiences increased mobility when bound to R380C tubulin (Figure 3, C and E).

### TUBB3-R380C increases kinesin-dependent transport in cells.

The kinesin motor domain and tubulin, along with the region around arginine-380 in β-tubulin, are highly conserved (Tischfield et al., 2010). Consistent with this strong conservation, our data show that the R380C substitution in yeast tubulin not only enhances microtubule localization of the kinesin Kip3 in yeast but also increases the binding and transport activity of mammalian Kif21a. We next investigated if the kinesin-boosting effect of R380C is conserved in human tubulin and whether the substitution would impact kinesin-dependent transport in a cellular context. To address these questions, we quantified kinesin-dependent peroxisome transport in Drosophila S2 cells (Ally et al., 2009).

The CFEOM-causing R380C and D417H mutations have been described in human  $\beta$ -tubulin isotype Tubb3. Thus, we transfected S2 cells with constructs encoding either wildtype human Tubb3, Tubb3-R380C, or Tubb3-D417H to quantify the effects of the mutant tubulin on peroxisome movements. In S2 cells peroxisomes are transported toward microtubule plus-ends by kinesin-1, while dynein is responsible for minus-end directed movements (Kural et al., 2005). To focus only on microtubule-dependent transport, we treated cells with cytochalasin D to depolymerize the actin cytoskeleton and eliminate any contribution from actin-dependent motors. S2 cells treated with cytochalasin D develop many-micron long, microtubule-rich extensions (Figure 4A; Lu et al., 2013). These long, thin projections have been shown to contain polarized microtubules organized with their minus-ends toward and plus-ends projected

FIGURE 3: β-tubulin-R380C allosterically impacts kinesin regions critical for chemomechanical activity and processive motility. (A) Ribbon and space filling model of kinesin (Kif5b) bound to tubulin. β-tubulin-R380 (blue) is positioned away from the binding interface. Kinesin  $\alpha 4$  (magenta) and  $\alpha 6$  (cyan) helices and ATP (gold) are colored. (B) Two different views of kinesin highlighting in various colors structural elements critical for chemomechanical activity and processive motility. (C) RMSF of amino acids in the structure of kinesin-ATP bound to wildtype versus R380C microtubules. (D and E) Views of kinesin highlighting regions of altered RMSF (red) that are either (D) not known to be important or (E) critical for kinesin activity. ATP shown in yellow and neck linker in black. (F) Schematic model of kinesin structural changes during chemomechanical cycle. Top row: When not bound to the microtubule, ADP-bound kinesin stochastically undergoes seesaw motion with the bulky side chains (L258, L261) of the  $\alpha$ 4 helix (magenta) acting as the "fulcrum" (triangle; Sindelar and Downing, 2010). Bottom row: Microtubule binding of the leading kinesin head positions the  $\alpha$ 4 helix along the interface of the  $\alpha$  and  $\beta$ -tubulin subunits and promotes extension of the N-terminal end of the helix (light magenta) and structural ordering of the loop 11/switch II motif (L11; orange), which sterically hinders seesaw motion and keeps the neck linker (NL; green) in the disordered configuration. In the ATP bound state, kinesin seesaws into the alternate configuration with a movement of  $\alpha$ 6 helix (blue) relative to  $\alpha$ 4, and an extension of the C-terminal end of  $\alpha$ 6 (green) that allows the connected neck linker to dock along the motor domain in the ordered conformation (solid green line), generating the power stroke to thrust the previously trailing motor head into the leading position. (Fourniol and Moores, 2010; Sindelar and Downing, 2010; Gigant et al., 2013; Atherton et al., 2014; Shang et al., 2014).

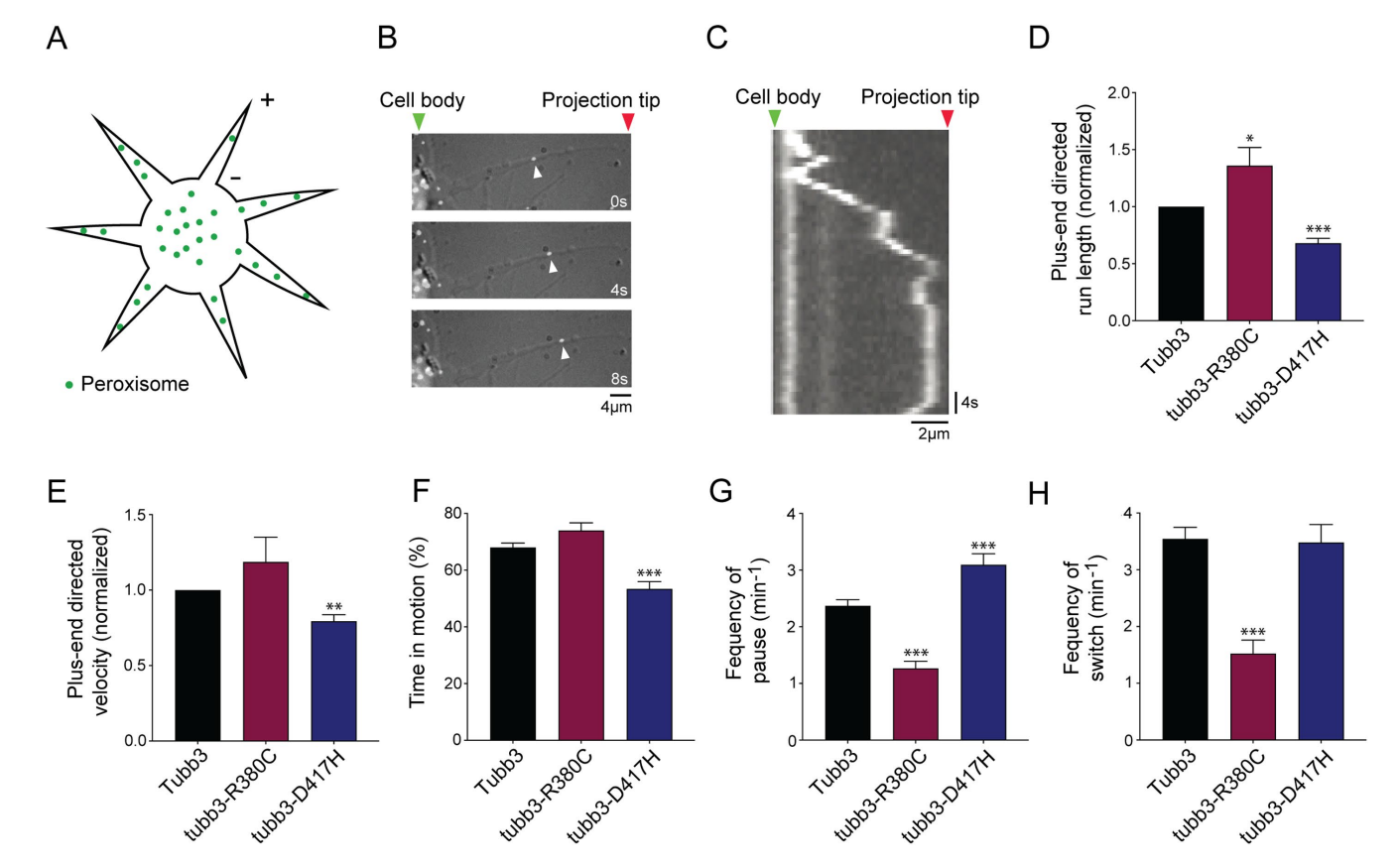


FIGURE 4: TUBB3-R380C increases kinesin-dependent transport in S2 cells. (A) Schematic of GFP-labeled peroxisomes (green circles) in cytochalasin D-treated S2 cells. (B) Snapshots from time-lapse images of GFP-labeled peroxisome (white, arrowhead) in S2 cell projection. (C) Representative kymograph of peroxisome transport in S2 cell projections. (D–H) Parameters of peroxisome transport in cells expressing wildtype Tubb3, Tubb3-R380C, or Tubb3-D417H as indicated. Expression of wildtype Tubb3 did not significantly alter peroxisome transport compared with control S2 cells lacking Tubb3 expression (see Supplemental Figure S4). In (D) run length for Tubb3 =  $0.5387 \pm 0.025 \,\mu\text{m}$  (mean  $\pm$  SEM) and in (E) velocity =  $0.148 \pm 0.006 \,\mu\text{m/s}$  (mean  $\pm$  SEM). For Tubb3, Tubb3-R380C, and Tubb3-D417H in (D) n = 1121, 216, and 494, in (E) n = 1119, 216, and 492, in (F) n = 235, 63, and 108, in (G) n = 235, 63, and 108, and in (H) n = 206, 63, and 108 from 51, 29, and 35 cells, respectively, from at least two independent experiments. For all panels graphs depict mean  $\pm$  SEM; asterisks denote p values compared with Tubb3; \*  $p \le 0.05, ** p \le 0.01,$  and \*\*\*  $p \le 0.001$  by unpaired Student's  $p \le 0.001$  b

outward from the cell body (Kural et al., 2005). We monitored anterograde movement of GFP-labeled peroxisomes within the projections by time-lapse microscopy and quantified parameters of kinesin-dependent transport on microtubules (Figure 4, B and C; Ally et al., 2009).

Relative to wildtype Tubb3, in cells expressing Tubb3-R380C the plus-end directed run length, defined as a segment of continuous peroxisome movement, is increased by 35% (Figure 4D). In cells expressing Tubb3-D417H it is decreased by ~30% (Figure 4D). While R380C does not significantly alter the velocity of peroxisome movement, D417H markedly reduces the speed of transport (Figure 4E). The distribution of cellular projection lengths in cells expressing the R380C or D417H mutants are comparable to those in cells expressing wildtype Tubb3 (Supplemental Figure S4A). Thus, potential differences in projection lengths cannot explain the observed increase and decrease of peroxisome run lengths on R380C and D417H microtubules, respectively. The D417H substitution also reduces the percent time peroxisomes spend in motion, which is countered by an increased frequency of changing from a moving to stationary state, or pausing, and total time spent paused (Figure 4, F and G; Supplemental Figure S4B). The R380C substitution, in contrast, decreases the frequency of peroxisome pausing by 50% (Figure 4G). Peroxisomes traveling on Tubb3–R380C microtubules also continue traveling in the same direction longer than they do on wildtype Tubb3 microtubules (Figure 4, G and H). We did not observe a noticeable accumulation of peroxisomes at the tips of projections in cells expressing R380C compared with wildtype Tubb3. Notably, none of the transport parameters are significantly altered between control S2 cells and those expressing wildtype Tubb3 (Supplemental Figure S4, C–H).

These data show that relative to wildtype Tubb3, the D417H substitution diminishes kinesin-dependent peroxisome movement. This is consistent with previous reports showing reduced kinesin localization to D417H-containing microtubules in yeast and mouse cells, as well as decreased transport of vesicles and mitochondria in mouse hippocampal neurons (Tischfield *et al.*, 2010; Niwa *et al.*, 2013). Opposite to the effect of D417H, and consistent with the increased kinesin localization observed in yeast cells, the R380C substitution enhances kinesin-dependent peroxisome transport when expressed in S2 cells. Finally, both mutations alter peroxisome movement in a dominant manner.

Altogether these results show that substitution of the conserved arginine 380 residue with cysteine increases multiple parameters of

kinesin activity resulting in boosted kinesin-dependent transport in a cellular context. Conversely, most parameters of kinesin-dependent transport are decreased by the D417H mutation.

# Molecular modeling reveals more effective protofilament-aligned motion on R380C microtubules

To examine the molecular motions of kinesin bound to the microtubule we built a model of the Kif5b kinesin motor domain bound to a segment of 13 protofilament microtubule assembled from either wildtype or R380C Tub1/Tub2 tubulin heterodimers (See Supplemental Material). Elastic network modeling with NOLB (nonlinear rigid block normal mode analysis) is used to reveal the normalmode of protein motions, with the first few modes likely representing the action of the most prevalent movements (Hoffmann and Grudinin, 2017). This approach using the entire kinesin-microtubule structure reveals that the first three modes of internal motions of the kinesin relative to the microtubule are a longitudinal "rocking" (Supplemental Movie 1), a lateral "tilting" (Supplemental Movie 2), and a "twisting" that reflects a rotation of the motor domain relative to the underlying tubulin subunit (Supplemental Movie 3). Consistent with this, a tilting motion of  $\sim$ 12–15° has been proposed as a key component of the ATP-dependent enzymatic cycle of kinesin from static structures (Figure 3F; Sindelar and Downing, 2010; Gigant et al., 2013; Atherton et al., 2014; Shang et al., 2014). Our results further reveal that the directionality of the primary kinesin motions is significantly altered on R380C microtubules (Figure 5). By using a reference vector that connects the centers of adjacent tubulin heterodimers along a single protofilament, it is seen that the longitudinal rocking motion is offset by 52° on wildtype but only 11° on the R380C microtubules. Thus, the direction in this rocking motion is nearly parallel to the protofilament when kinesin is bound to the R380C polymer (Figure 5A), that is, more aligned with the direction of translocation. On the wildtype microtubules the tilting motion is offset by 43° from this reference vector, while on R380C it is nearly perpendicular with an 88° offset (Figure 5B). The direction of the twisting motion is altered relatively little with an overlap of 35% for wildtype and 30% for the R380C microtubules, respectively (Figure 5C).

Strikingly, when the first 100 normal modes of kinesin motion are considered, the overlap of the cumulative motion with the longitudinal reference vector on wildtype microtubules is 23.5%. On R380C microtubules, cumulative kinesin motion is more aligned with the protofilament and overlap with the reference vector increases to 62.1%. This indicates a significant change in the direction of the net cumulative motion with longitudinally-directed motions of the motor domain favored on R380C in comparison with wildtype microtubules. Altogether, the computations show that R380C induces allosteric changes in kinesin and enhances the processivity-directed motion of the kinesin-microtubule interaction.

# DISCUSSION

Kinesins and microtubules exploit a highly conserved interaction to underlie a wide range of biological functions. Our data show that the R380C substitution in yeast  $\beta$ -tubulin enhances kinesin localization on microtubules in budding yeast. It also increases multiple parameters of mouse Kif21a activity on these microtubules in vitro. Additionally, the same R380C substitution in human  $\beta$ -tubulin, when expressed in Drosophila S2 cells, promotes kinesin-dependent peroxisome transport. One possible limitation of our study may be the use of yeast tubulin to measure mammalian Kif21a activity in vitro and for MD simulations in silico. Differences between yeast and human tubulin could potentially influence the allosteric mechanism

proposed here for regulation of kinesin activity by the R380C substitution. Yet, the enhanced kinesin activity is observed with tubulins and kinesins from multiple species, that is, mouse or Drosophila kinesin with yeast or human tubulin, respectively. Thus, these differences may also be a strength, revealing a conserved effect of R380C on kinesin motor activity. This is in stark contrast to the conserved impact of D417H which, like R380C, also causes CFEOM but severely diminishes kinesin activity in all these contexts.

The kinesin motor domain, tubulin, and specifically  $\beta$ -tubulin residues R380 and D417 are highly conserved (Tischfield et al., 2010). The D417H substitution disrupts a conserved interaction at the tubulin-motor interface needed for tight kinesin binding to the microtubule (Uchimura et al., 2006). Our data show that R380C also alters conserved tubulin-motor interactions, but in a manner that enhances productive binding and kinesin activity. Substituting βtubulin R380 with any amino acid does not produce the same effect. In contrast to R380C, the R380A mutation does not alter the in vitro binding frequency, run length, or velocity of HK560, a truncated human kinesin-1 construct (Uchimura et al., 2010). Yet it lowers the microtubule binding strength of the nucleotide free- and AMP-PNPbound form of the kinesin, while increasing the unbinding force relative to the stall force of the AMP-PNP-bound motor. Thus arginine 380 may influence microtubule-kinesin interactions in a nucleotidesensitive manner, while the substitution with alanine or cysteine differentially affects this allosteric communication.

### β-tubulin-R380C increases kinesin activity by a dominant mechanism that is different from that of CFEOM-causing Kif21a mutations

While CFEOM-causing mutations in Kif21a activate the mutant motor on wildtype microtubules, the β-tubulin-R380C mutation conversely activates wildtype kinesins on the mutant polymer. Although both scenarios result in CFEOM, the underlying mechanisms of kinesin activation are distinct. Mutations in Kif21a function to attenuate the intramolecular head-to-tail interactions that normally autoinhibit the motor (Cheng et al., 2014). In contrast, the effect of β-tubulin-R380C is observed independent of tail-mediated autoinhibition. Relative to full-length motor, the basal activity of tail-truncated Kif21a-917, which lacks autoinhibition, is increased on normal microtubules. Notably, Kif21a-917 activity is further enhanced on β-tubulin-R380C microtubules (Figures 1 and 2). This excessive activation is independent of the kinesin tail, and thus the head-to-tail autoinhibition mechanism. Instead, kinesin activation by  $\beta$ -tubulin-R380C is likely mediated through the motor domain.

We cannot exclude the possibility that, rather than  $\beta$ -tubulin-R380C enhancing kinesin activity directly, another factor present in the tubulin preparations or HEK293T and S2 cells stimulates motor activity in the context of R380C microtubules. A contaminating protein(s) enriched in the R380C tubulin preparation could function to enhance kinesin activity. Alternatively, a factor present in all tubulin preps, or in the HEK293T cell lysates could increase motor activity specifically on R380C microtubules. However, a factor similarly capable of boosting kinesin transport specifically on R380C tubb3containing microtubules would also be required in S2 cells, which decreases the likelihood of this scenario. Thus, we favor the hypothesis that R380C directly impacts kinesin function.

Unlike  $\beta$ -tubulin D417, the R380 residue is not located at the microtubule-motor binding interface. Instead, it lies on the underside of helix  $\alpha$ 11 on  $\beta$ -tubulin (Figure 3A). Thus, it does not directly contact kinesin. Previous work showed that, although Tubb3-R380C folds less efficiently than wildtype in reconstituted in vitro transcription/translation assays, R380C mutant tubulin heterodimers are

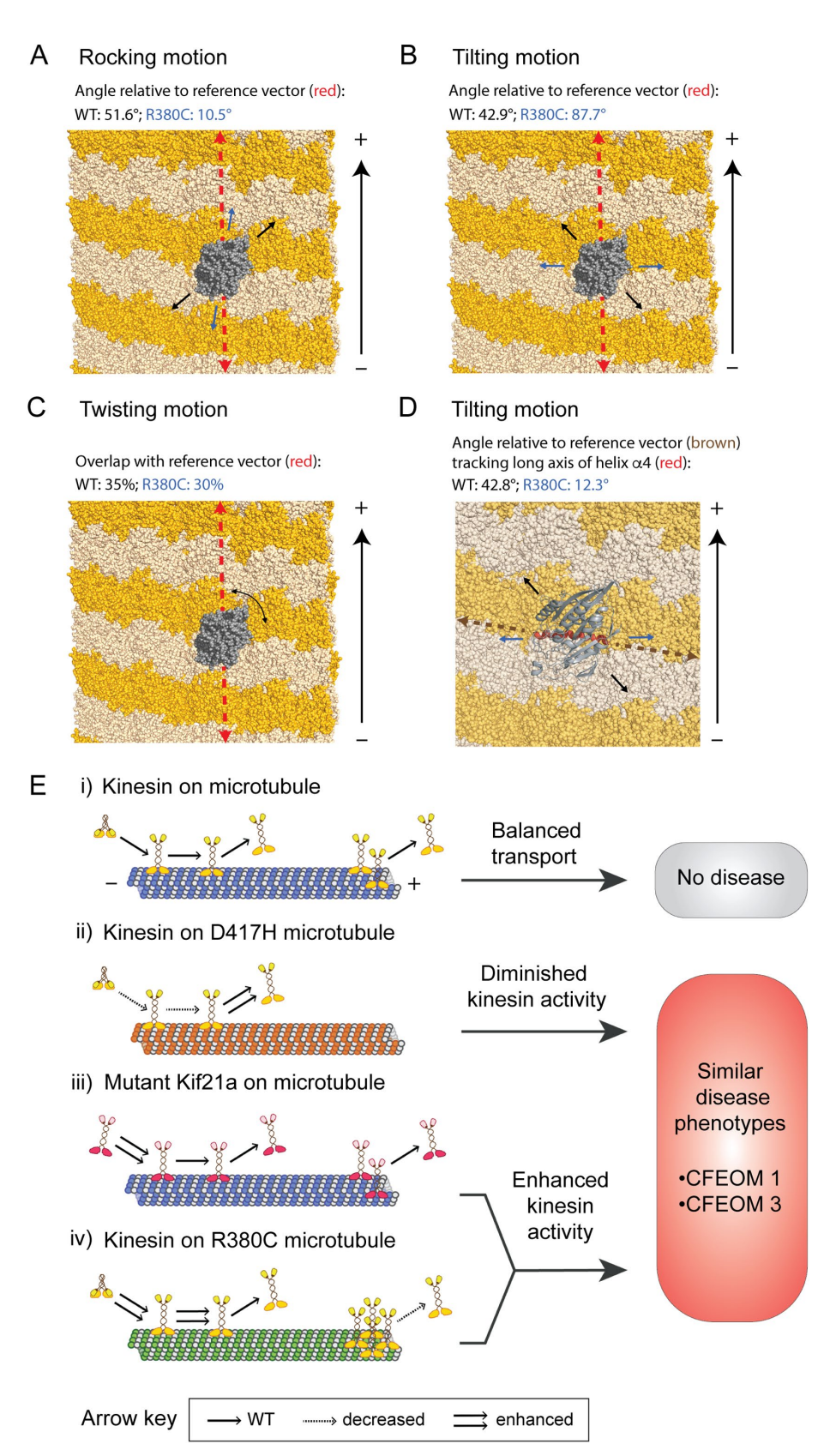


FIGURE 5:  $\beta$ -tubulin-R380C allosterically alters motions of the motor domain during kinesin-microtubule interaction, and a unifying model for tubulin and Kif21a CFEOM mutations. (A–D) Change in the first three modes of nonrigid body kinesin motion when bound to wildtype versus R380C microtubules. Structure of kinesin (Kif5b) bound to microtubule with plus-end at top. The approximate direction of the indicated kinesin motion is depicted on wildtype (black arrows) and R380C (blue arrows) microtubules. (A and B) A longitudinal reference vector intersecting tubulins

nonetheless formed in vivo and copolymerize into cellular microtubules (Tischfield et al., 2010). In our yeast assay the diploid cells are heterozygous for  $\beta$ -tubulin-R380C or -D417H, thus each represents only a fraction of cellular tubulin yet is sufficient to alter microtubule-kinesin interaction. For in vitro TIRF assays tubulin was purified from cells overexpressing wildtype  $\alpha$ -tubulin and mutant  $\beta$ -tubulin, which leads to enrichment of the overexpressed, mutant heterodimers (Johnson et al., 2011). In the S2 cell assays, TUBB3 was transiently expressed in the presence of the full complement of Drosophila β-tubulins. Quantitative immunostaining revealed cells transfected with wildtype or mutant TUBB3 expressed ~5% more total tubulin than those nontransfected (see Materials and Methods). Thus, Tubb3-R380C likely comprises a limited proportion of the microtubule subunits. Nevertheless, even at these levels it increases

in the same protofilament shown as dashed red arrow. The angle of the kinesin motion relative to the reference vector is indicated for each case. (C) The directionality of twisting motion on the microtubule is indicated by the curved arrow. The percent overlap of the twisting motion with the longitudinal reference vector on wildtype and R380C microtubules is indicated. (D) The angle of kinesin "tilting" motion relative to a reference vector (brown) tracking the long axis of  $\alpha$ 4 (red) is indicated for wildtype and R380C microtubules. (E) A unifying model for tubulin and Kif21a CFEOM mutations. (i) Intracellular transport levels are balanced when wildtype kinesin operates on wildtype microtubules in healthy axons. (ii) Tubb3-D417H and other  $\beta$ -tubulin mutations diminish kinesin transport in axonal compartments and result in CFEOM (Tischfield et al., 2010; Cederquist et al., 2012; Niwa et al., 2013; Minoura et al., 2016). (iii) Kif21a mutations that have been examined increase its activity on wildtype microtubules in axons and cause CFEOM (Cheng et al., 2014). (iv) Tubb3-R380C also increases kinesin-dependent transport in axons and produces CFEOM. Notably, there are multiple scenarios in which excess kinesin activation could lead to diminished cargo delivery in axons (see discussion). Kif21a mutations primarily cause isolated CFEOM (Yamada et al., 2003), while those in tubulin mainly cause CFEOM with additional axon disorders (Tischfield et al., 2010; Cederquist et al., 2012), presumably because disrupting Kif21a predominantly affects its cargoes, whereas altering the microtubule can perturb the delivery of materials by a range of kinesins, as well as microtubule dynamics and interaction with MAPs. See also Supplemental Movies S1-4.

kinesin-dependent peroxisome transport. These findings are consistent with the observation that R380C and D417H both demonstrate gain-of-function mechanisms and cause disease while comprising only a fraction of cellular β-tubulin (Tischfield et al., 2010). Considering its position away from the binding interface, the R380C substitution most likely introduces structural changes that allosterically impact motor function. The fact that it acts at substoichiometric levels suggests R380C may potentially influence neighboring tubulin subunits to enhance kinesin activity on the surrounding polymer. Indeed, there is emerging evidence that allosteric communication within the microtubule can drive cooperative kinesin binding and processivity (Peet et al., 2018; Shima et al., 2018; Wijeratne et al., 2022).

R380C does more than simply increase the binding affinity of Kif21a, as in vivo and in vitro assays show it enhances multiple parameters of kinesin activity. Rather than gain efficiency in a specific aspect of the enzymatic cycle, R380C may bolster the overall chemomechanical process. In other words, it enhances the coordinated cycle between the two motor heads needed for processive motility. The R380C microtubule serves as a better substrate, or partner, for kinesin transport. Because the R380 residue does not contact kinesin directly, this is likely accomplished via allosteric effects.

# The β-tubulin-R380C substitution allosterically induces changes in bound kinesin

There are two major categories of molecular motions required for processive kinesin motility. In the first category, conformational changes within the motor domain link the microtubule interaction status with ATP binding and hydrolysis (Sindelar and Downing, 2010; Gigant et al., 2013; Atherton et al., 2014; Shang et al., 2014; Benoit et al., 2021). In the second category, the changes within a motor domain are coupled with the larger scale molecular motions needed to coordinate the binding and release of the two motor domains to the microtubule (Toprak et al., 2009; Hancock, 2016). Our molecular modeling shows  $\beta$ -tubulin-R380C allosterically impacts both categories of kinesin motion. First, our MD simulations reveal RMSF changes concentrated in elements that are critical for the kinesin chemomechanical cycle, namely helices  $\alpha 4$ ,  $\alpha 6$ , and loop 11/switch II. During the chemomechanical cycle, binding of the motor to the microtubule both licenses that motor domain for ATP binding and hydrolysis, as well as promotes release of the other, now trailing head (Hancock, 2016). Helix  $\alpha 4$  constitutes the major binding element, and microtubule binding status is transmitted from  $\alpha 4$  to the nucleotide binding pocket via loop 11, which itself makes up part of the Switch II motif. Microtubule binding induces extension and stabilization of the end of  $\alpha 4$ , also known as the switch relay, leading into loop 11 (Gigant et al., 2013; Atherton et al., 2014; Shang et al., 2014). This in turn stabilizes loop 11 in a short helical structure that converts switch II to the closed, or ATP hydrolysis-competent state (Gigant et al., 2013; Atherton et al., 2014; Shang et al., 2014). Our RMSF data indicate that R380C stabilizes loop 11 in the microtubule-bound confirmation (Figure 3). This could serve to promote microtubule binding and/or more efficiently couple microtubule interaction to ATP binding and/or hydrolysis. Although it is debated whether ATP binding or hydrolysis is the trigger, it is widely held that this leads to a critical rearrangement of the neck linker connecting the two motor domains that propels the freshly detached trailing motor ahead of the tightly bound leading domain, thus positioning it to locate the next available tubulin subunit (Hancock, 2016; Benoit et al., 2023). This rearrangement, or "docking" of the neck linker requires coordinated movements of  $\alpha 6$  and  $\alpha 4$ , at the end opposite

to loop 11 (Figure 3F; Gigant et al., 2013; Atherton et al., 2014; Shang et al., 2014). Our modeling reveals that R380C promotes increased flexibility specifically in these elements (Figure 3). This flexibility may simply allow the neck linker to more readily reposition upon ATP binding or hydrolysis. It's also possible, however, that productive microtubule binding specifically induces flexibility in these elements to facilitate neck linker repositioning. Similarly, productive microtubule binding may further reinforce the stabilization of loop 11 to promote ATP hydrolysis. Together our activity assays and molecular modeling show that R380C induces structural changes in tubulin that allosterically influence key chemomechanical elements in kinesin and that this influence is likely responsible for enhancing motor transport.

Our elastic network modeling of kinesin interacting with the microtubule further reveals that R380C impacts the second category of movements, the large-scale motions that coordinate the enzymatic cycles of both motors to produce processive motility. Notably, during the chemomechanical cycle, a kinesin tilting motion plays a key role linking microtubule binding and nucleotide status, via  $\alpha 4$  and loop 11, to changes in α6 and neck linker docking (Figure 3F; Sindelar and Downing, 2010; Gigant et al., 2013; Atherton et al., 2014; Shang et al., 2014). This tilting creates a "seesaw" effect of the motor relative to  $\alpha 4$  and tubulin. The tilting motion we observe could facilitate this seesaw motion and, indeed, the amplitude of overall motor domain tilting exceeds that of  $\alpha 4$  itself relative to the underlying microtubule (Supplemental Movie S4). Moreover, on wildtype microtubules the tilting motion is offset from a vector tracking the long axis of  $\alpha 4$  by 43°, but on R380C the offset is reduced to only 12° (Figure 5D). Thus, R380C may promote efficient chemomechanical coupling between microtubule binding, ATP hydrolysis, and neck linker docking.

For the chemomechanical cycles of both motors to remain coordinated during processive motility there must be communication between them. This is likely transmitted via strain through the connecting neck linker or through the microtubule polymer, or a combination thereof. During a processive step, the newly trailing head is already tightly bound to the microtubule and, thus, unlikely to engage in a rearward motion to introduce strain through the neck linker. The newly leading head, on the other hand, could readily undergo forward or rotational movement upon tight microtubule binding to produce tension through the neck linker and signal the trailing head to detach. The rotational motion we detect by elastic network modeling could facilitate a movement that extends the neck linker (Figure 5C). Such a rotation by the leading head would also displace the tether location plus-endward and could account for the counterclockwise torque observed in the kinesin stepping mechanism (Yajima and Cross, 2005). Finally, the longitudinal motion of kinesin is highly aligned with the protofilament on R380C compared with wildtype microtubules. Movement along this vector could facilitate trailing motor detachment when it comes under pulling forces as the leading head establishes tight binding. Overall, the cumulative direction of the first 100 normal modes of motion clearly demonstrates R380C has a significant impact on kinesin movement. More specifically, the first three modes are altered in a manner consistent with enhanced kinesin activity and processive motility. These elastic network modeling results further support a model in which R380C induces allosteric changes in bound kinesin that promote enhanced motor activity and transport.

The role of microtubule allostery in supporting kinesin function is becoming clear. Multiple studies suggest that kinesin binding can allosterically alter microtubule structure to promote binding and processivity of other motors in the region (Vilfan et al., 2001;

Muto et al., 2005; Shima et al., 2018; Wijeratne et al., 2022). Such cooperative binding may at least partially underlie the preferential use of subsets of microtubules for directional transport (Nakata and Hirokawa, 2003; Reed et al., 2006; Nakata et al., 2011; Tas et al., 2017; Shima et al., 2018). Our data now show that the microtubule itself can influence the kinesin traveling on it. Thus, there is bidirectional allosteric regulation between the microtubule and kinesin, which can likely be transmitted through neighboring tubulin subunits within the microtubule. This further supports the idea that during processive motility, the binding status of the two motor domains is communicated, at least in part via the microtubule, perhaps by enhancing neck linker strain or by promoting various conformational or interaction states.

The increased binding and productive encounter frequencies resulting from R380C suggest it favors a tubulin conformation that is needed for efficient chemomechanical cycling of kinesin. If so, why have microtubules not adapted to this more optimal conformation? One potential reason may be that doing so would compromise the structural integrity of tubulin, or the microtubule, that is necessary under some conditions. Another likely explanation is that microtubules must support a range of activities, and further optimizing kinesin function may concomitantly perturb other function(s) (Nsamba et al., 2021). Suboptimal kinesin function may be a limitation imposed by the need to accommodate the molecular mechanisms of other important microtubule-associated proteins (MAPs) and regulatory factors.

# Decreased or increased kinesin activity results in similar disease phenotypes

Our findings reveal that, similarly to CFEOM-causing Kif21a mutations, those in Tubb3 can also enhance kinesin transport. Kif21a CFEOM mutations in mice and humans increase microtubule binding along with the percent encounters that result in productive motility (Cheng et al., 2014; Bianchi et al., 2016). Tubb3 mutations also cause CFEOM in mice and humans, yet in sharp contrast they generally disrupt kinesin interaction with microtubules (Tischfield et al., 2010; Minoura et al., 2016). R380C resolves this dichotomy and reveals that while the majority of CFEOM-causing mutations in tubulin genes decrease kinesin activity, for instance D417H, a subset of Tubb3 mutations enhance kinesin-mediated transport. Altogether this strengthens the paradigm that altered kinesin activity underlies the mechanism(s) driving tubulin-associated CFEOM (Figure 5E). One significant difference is that while mutations in Kif21a result primarily in CFEOM, those in Tubb3 and Tubb2b cause CFEOM accompanied with a spectrum of additional neuronal phenotypes that generally segregate with the specific substitution (Tischfield et al., 2010; Chew et al., 2013; MacKinnon et al., 2014; Balasubramanian et al., 2015; Whitman et al., 2014, 2016).

There are several potential reasons why tubulin CFEOM mutations display a broad spectrum of neuronal phenotypes. Compared to Kif21a mutations, which likely affect cargoes of that motor, changes to the underlying microtubule tracks produced by tubulin mutations could influence the materials transported by a range of kinesins. Mutations may also differentially influence specific kinesins, resulting in unique imbalances in their cumulative activities. Many CFEOM tubulin mutations, including R380C, also affect the dynamic properties of microtubules (Tischfield et al., 2010). Additionally,  $\beta$ -tubulin-R380C makes direct interactions with doublecortin (DCX), a neuronal-specific MAP important for healthy brain development (Cushion et al., 2013; Cook et al., 2020). Several other mutations are known to influence MAP binding (Hoff et al., 2022; Cushion et al., 2023). Thus, the observed phenotypic

spectrum may reflect various combinations of altered microtubule dynamics, MAP function and kinesin activities. Similar aspects likely explain why Kif21a mutations mainly result in CFEOM type 1 while those in Tubb3 and Tubb2b produce type 3, distinguished by distinct patterns of failed ocular muscle innervation (Yamada et al., 2004; Whitman et al., 2014).

Our results bolster an emerging body of evidence linking either inhibited or excessive kinesin activity to similar disease states. The majority of tubulin CFEOM mutations disrupt kinesin activity yet, Kif21a mutations promote CFEOM by a gain-of-function mechanism activating transport (Tischfield et al., 2010; Cederquist et al., 2012; Niwa et al., 2013; Cheng et al., 2014; Bianchi et al., 2016; Minoura et al., 2016). We now show β-tubulin-R380C activates kinesin, through a different molecular mechanism, and also produces CFEOM. A similar relationship is seen with hereditary spastic paraplegia (HSP), which can result from mutations in the kinesin-3 family members Kif1a and Kif1c (Gabrych et al., 2019). While many kinesin-3 HSP mutations are loss of function and inhibit activity (Lee et al., 2015; Nieh et al., 2015; Cheon et al., 2017), several are gainof-function producing increased binding rates and hypermotility (Chiba et al., 2019). Additionally, Kif21b mutations that result in neurodevelopmental disorders associated with brain malformations and microcephaly (Asselin et al., 2020), and mutations in Kif5a that cause amyotrophic lateral sclerosis, or ALS (Baron et al., 2022; Soustelle et al., 2023), were recently shown to relieve autoinhibition and activate transport by these motors. It is readily apparent how loss of kinesin-mediated transport can disrupt cellular processes and cause disease. These recent results reveal the hazards of excessive kinesin activity, and highlight the importance of balance, or homeostasis, in microtubule-mediated transport systems for cellular and organismal health.

There are multiple models for how increased kinesin activity could disrupt cellular homeostasis. It may simply deliver excessive cargo that, at increased concentration, overwhelms signaling pathways or disrupts downstream mechanisms. Problems could also result if the complementary transport systems, such as dynein, cannot sufficiently deliver increased payloads, including plus-end directed motors, back toward microtubule minus-ends. Increased transport activity could possibly result in "traffic jams" within the axon, decreasing overall efficiency. Alternatively, prematurely active kinesins may depart without sufficient cargo loading and effectively result in deficient delivery. Moreover, constitutively active kinesins may potentially be resistant to dynein-mediated recycling, resulting in a dearth of available kinesin motors in cargo-loading areas, again causing deficient delivery. It is striking how inhibition or increased activity of kinesin are associated with similar phenotypes, but also noteworthy that several of these models of increased activation may, like inhibition, lead to diminished delivery. Charcot-Marie-Tooth disease type 2A is known to result from loss of function mutations in the kinesin Kif1b (Zhao et al., 2001) while additional mutations in a range of kinesins are at least genetically associated with various disease phenotypes, or so-called kinesinopathies (Kalantari and Filges, 2020). Although most remain uncharacterized, it may be important to determine the functions of these pathogenic mutations. This is likely to uncover additional activating mutations in kinesin and, quite likely, dynein motors (Marzo et al., 2019) resulting in human disease. With tubulin mutations, it will be important to determine whether specific substitutions affect all kinesins to a similar extent, or differentially influence unique subsets of motors. Such knowledge will provide valuable insights for understanding the cellular etiology of the TUBB3 syndromes as well as other tubulinopathies.

#### **MATERIALS AND METHODS**

### Construction of plasmids and yeast strains

Plasmids for galactose-induced overexpression of wildtype yeast tubulin containing an internal polyHis affinity tag on  $\alpha$ -tubulin (Tub1) were previously described (Sirajuddin et al., 2014). The R380C and D417H mutations were introduced into β-tubulin (Tub2) on these plasmids using Quickchange site-directed mutagenesis (Agilent Technologies) and verified by Sanger sequencing. The  $\alpha$ -tubulin plasmid, GAL-TUB1(His)-URA3, and specific wildtype or mutant βtubulin plasmid, GAL-TUB2-TRP1, were co-transformed into wildtype diploid yeast for overexpression of the desired tubulin variant. Plasmids for expression of GFP-tagged mouse Kif21a, either full length (Kif21a) or truncated (Kif21a-917) were previously described and used without modification for expression in HEK293T cells (Cheng et al., 2014). To generate plasmids for Drosophila S2 cell peroxisome motility assays, the wildtype human TUBB3 gene was amplified by PCR from the Marathon-ready human fetal brain cDNA library (Clontech) without the stop codon. The gene was then recombined into the DONR221 (Invitrogen) vector before subcloned into pcDNA3.2/V5-DEST (Invitrogen) in-frame with the C-terminal V5 epitope tag and with the start codon in the context of a suboptimal Kozak sequence. The final sequence was verified by Sanger sequencing. Disease-associated mutations were introduced using site-directed mutagenesis (Agilent Technologies) and the entire gene sequence reverified. For expression in S2 cells, the tubulin genes were subcloned into the pMT/V5-His A (Invitrogen) plasmid and the sequence reverified. The plasmid expressing Drosophila eGFP-SKL to visualize peroxisomes in S2 cells was previously published (Kural et al., 2005; Lu et al., 2013). Yeast strains used for localization of Kip3-3YFP on wildtype, R380C and D417H microtubules marked with CFP-Tub1 ( $\alpha$ -tubulin) were also described previously (Tischfield et al., 2010).

### Quantification of Kinesin localization in yeast cells

Kip3-3YFP localization on astral microtubule plus-ends was quantified as done previously (Cederquist et al., 2012). Briefly, cells expressing KIP3-3YFP and CFP-TUB1 were grown to log phase at 30°C in SC media with 0.2 mM adenine, then imaged at room temperature on a Zeiss Axiolmager M2 microscope using a 63X Pan Fluor 1.4 N.A. objective leading to a Coolsnap HQ2 camera (Photometrics). Three-dimensional stacks encompassing the cell were acquired at 0.75 µm step size and used to make maximum projection images in which all identifiable CFP-microtubule plus-ends in G1 cells were marked with an equal-diameter circle. The YFP signal inside each circle was quantified and the average YFP background obtained from the cytosol was subtracted to determine the plusend associated Kip3-3YFP signal. The average Kip3-3YFP localization was obtained from four trials using two individual clones for each genotype. Images were captured and processed using Slide-Book software (Intelligent Imaging Innovations).

# Preparation of proteins for in vitro assays

Wildtype and mutant yeast tubulin was expressed and purified essentially as previously described (Johnson et al., 2011). Briefly, haploid yeast cotransformed with high copy plasmids encoding GAL1-TUB2(6xHis)-URA3 and GAL1-TUB2-TRP1 (or mutant TUB2) was grown in selective medium (CSM-Ura-Trp) overnight and used to inoculate 2 × 15 L of YPGL (2% peptone, 1% yeast extract, 3% glycerol, 2% lactate) at a ratio 1:15 (inoculum:YPGL). Each 16 L culture was grown in a plastic carboy with aeration at 30°C for 24 h before adding galactose at 2% final concentration, to induce tubulin expression from the GAL1 promoters. After an additional 8 h at 30°C with

aeration, cells were harvested, washed with water, snap frozen in liquid nitrogen and stored at -80°C. For tubulin purification cell pellets were thawed and resuspended at 50% wt/vol in ice cold lysis buffer (50 mM HEPES pH 7.4, 500 mM NaCl, 10 mM MgSO<sub>4</sub>, 30 mM imidazole, 1 mM PMSF, 50  $\mu$ M GTP), then lysed by 10 passes through a microfluidizer. Cell lysates were centrifuged 30 min at 17,000g at 4°C to remove cell debris. All subsequent steps were carried out at 4°C and fractions were kept on ice. The clarified cell lysate was mixed with 10 ml Ni-NTA resin and incubated 30 min with tumbling. The volume was split and resin loaded onto two gravity columns with the flow through reapplied once onto the column. The resin was washed first with lysis buffer without PMSF, then with low salt buffer (25 mM HEPES pH 7.4, 1 mM MgSO<sub>4</sub>, 30 mM imidazole, 50 μM GTP). Finally, protein was released with elution buffer (25 mM PIPES pH 6.9, 1 mM MgSO<sub>4</sub>, 250 mM imidazole, 50 µM GTP). Fractions containing protein were pulled together and applied onto a 1 ml Mono S column (GE Healthcare) preequilibrated with binding buffer (25 mM PIPES pH 6.9, 2 mM MgSO<sub>4</sub>, 1 mM EGTA, 50 µM GTP). After washing with the same buffer, protein was eluted with a 30-column volume linear gradient of NaCl (buffer A: 25 mM PIPES pH 6.9, 2 mM MgSO<sub>4</sub>, 1 mM EGTA, 50  $\mu$ M GTP, buffer B: 25 mM PIPES pH 6.9, 2 mM MgSO<sub>4</sub>, 1 mM EGTA, 1 M NaCl, 50 µM GTP). Eluted fractions were analyzed by SDS-PAGE and those containing purified tubulin were pooled together and dialyzed against buffer A containing 200 mM NaCl and subsequently against buffer A. The purified tubulin was then concentrated using Amicon Ultra-4 centrifugal filters (3000 Da cut-off; Millipore). Protein concentration was measured using the Bradford method and 10% glycerol was added before snap freezing in liquid nitrogen. Tubulin was stored in liquid nitrogen until use.

Mouse Kif21a-GFP and Kif21a-917-GFP were expressed and prepared as previously described (Cheng et al., 2014). Briefly, vectors encoding GFP-fused full length or truncated Kif21a were transfected into HEK293T cells using lipofectamine. Approximately 40 h after transfection cells were lysed in BRB80 (80 mM K-PIPES, 1 mM EGTA, 1 mM MgCl<sub>2</sub>, pH6.8) supplemented with 2 mM Mg-ATP, 1% Triton, and protease inhibitor (Complete; Roche). Lysates were cleared by centrifugation at 100,000g at 4°C and then snap frozen in small aliquots and stored until use.

A rigor mutant of truncated, dimeric kinesin Kif5B fused with a C-terminal poly-lysine and 6xHis tags (K560-G234A-polyK-6xHis) was expressed in BL21 (DE3) cells at 24°C. Protein expression was induced for 9 h with 0.1 mM isopropyl β-D-1-thiogalactopyranoside (IPTG; Sigma-Aldrich). Purification was carried out at 4°C as previously described (Case et al., 1997; Rice et al., 1999) and 20% glycerol was added before snap freezing the kinesin in liquid nitrogen and storing at -80°C.

### In vitro TIRF microscopy assay

Microtubules were assembled from purified yeast tubulin at 2.3 µM final concentration supplemented with 8% rhodamine-labeled porcine tubulin (Cytoskeleton) at 30°C in polymerization buffer (BRB80; pH 6.8) with 2 mM GTP and 10% DMSO for 20 min. Subsequently, epothilone B was added to 20 µM and incubation continued for 30 min to stabilize microtubules before pelleting by centrifugation for 10 min at 100,000g. Microtubules were resuspended in warm polymerization buffer containing epothilone B and used the same day.

The kinesin motility assays were performed in microchannels prepared from glass coverslips and slides sealed with double-sided tape. Glass was precleaned using sequential rounds of sonication in detergent solution, 1M KOH, water, and then ethanol. Microchannels were equilibrated with BRB80, incubated with 1.75 µg/ml K560-G234A-polyK-6xHis in BRB80 for 20 min at room temperature, then washed with BRB80. They were then blocked with 8 mg/ml casein in 10 mM Tris-HCl, pH 8.0 for 10 min, washed with BRB80, then blocked with 1% Pluronic F127 and 0.05 mg/ml casein in BRB80 for 30 min at room temperature. Stabilized microtubules were diluted in polymerization buffer and 30 µl was introduced into an assay channel and incubated 10 min at room temperature to allow attachment. Unbound microtubules were washed away by perfusing with five channel volumes of polymerization buffer prior to equilibrating with another two channel volumes of motility buffer (30 mM K-PIPES pH 6.8, 2 mM MgCl<sub>2</sub>, 1 mM EGTA, 25 mM KCl, 1 mM DTT, 0.125 mg/ ml casein, 2 mM Mg-ATP). Full length mouse Kif21a-GFP or truncated Kif21-917-GFP was diluted in motility buffer also containing an oxygen scavenger mix (20 mM glucose, 200µg/ml glucose oxidase, 400μg/ml catalase, 0.5% β-mercaptoethanol) and 20 μM epothilone B, and three channel volumes perfused into the chamber. Alternatively, 100 mM KCl was included in the equilibrating and reaction mix for "high salt" conditions. Channels were sealed and incubated at 28°C in the dark for 10 min to allow reactions to reach steady-state. Assay chambers were used to record 2-4 time lapse images (2-s interval for 10 min) and discarded at a maximum of 60 min post kinesin addition.

Images were acquired using an Andor iXon3 897 EMCCD camera mounted on a Nikon ECLIPSE-Ti inverted microscope equipped with a CFI Apo 1.45 NA  $100 \times \text{oil}$  immersion TIRF objective (Nikon). A laser merge module (Spectral Applied Research) controlled excitation from 50 mW solid-state lasers (Coherent Technology) at 488 and 561 nm wavelengths delivered through fiber optics with a motorized TIRF illuminator at 7 and 2% laser power, respectively. An optical beam splitter was installed in the emission light path allowing for simultaneous imaging in both channels. Images were acquired every 2 s using 100 ms exposure and EM gain of 200.

To record photobleaching steps, full-length Kif21a-GFP or Kif21a-917-GFP was added to the flow chamber in PEM buffer. Unbound kinesin was washed out with 100  $\mu$ l PEM and molecules adhered to the coverslip surface were imaged on a Nikon TiE through-the-objective TIRF microscope using an ApoTIRF 1.49 NA 100  $\times$  oil immersion objective. 400 images were collected at a rate of 2 Hz on an Andor iXon888 EMCCD camera.

### Analysis of TIRF microscopy assay

Image analysis was performed using ImageJ software (Schneider et al., 2012). Briefly, tetraspec beads were used to calculate the offset and register the images between channels, and the timelapse images were subsequently drift-corrected. For analysis, only microtubules longer than 5 µm were included and at least two microtubules were randomly selected from each time-lapse and used to generate kymographs depicting kinesin signal intensity along the microtubule over time with ImageJ (Schneider et al., 2012). The binding rate of Kif21a-GFP and Kif21a-917-GFP on wildtype and mutant microtubules was determined by scoring the appearance of all new kinesin-GFP foci in the kymograph divided by the length of the microtubule and time encompassed by the kymograph. Processive movement was defined as kinesin moving > 0.17 µm in a directed manner after binding to the microtubule. Run length was determined by the distance of directed movement by kinesin along the microtubule. Velocity was defined as the distance traveled over time. Some kinesin display changes in instantaneous velocity during a single event, while some occasionally pause. Thus, velocity represents the time-averaged displacement of processive molecules. Pauses at the beginning or end of kinesin tracks were omitted. Dwell time was calculated as the time the kinesin remained associated with the microtubule after reaching the plus-end.

Instances in which more than one kinesin occupied the plus-end were excluded.

To analyze photobleaching steps, stationary fluorescent foci were manually identified and intensity plot profiles over time were generated for each single focus using ImageJ (Schneider et al., 2012). For each region, a neighboring area without detectable GFP signal was used to determine the background intensity that was subtracted from the intensity of each fluorescent focus. Foci that photobleached completely during the time-lapse were used to score the number of photobleaching steps in each focus.

### S2 cell transport assay

The S2 cell assay was performed as described previously (Kural et al., 2005; Lu et al., 2013). Drosophila S2 cells were maintained in Insect-Xpress protein free insect cell medium (Lonza, Walkersville, MD) at 25°C in a humidified incubator. On the day of transfection cells were plated in 24-well plates (Sigma, St. Louis, Missouri) and incubated at 25°C for ~1 h to allow adherence to the plate surface, then transfected using Effectene (Qiagen) according to the manufacturer's protocol with 4:1 M ratio of the tubulin expression plasmid to the pAC-eGFP-SKL plasmid (Kulić et al., 2008). Twenty-four hours posttransfection the expression of tubulin was induced by addition of 0.2 mM copper sulfate for 48 h. Cells were then replated onto Concanavalin A (ConA)-coated coverslips in medium containing 5 μM cytochalasin D to depolymerize actin filaments for 30 min. Time-lapse imaging of peroxisomes at 1 s intervals over 60 s was done with a Nikon U-2000 microscope with a  $100 \times 1.49$  N.A. lens, a 1.5X intermediate magnifier, and a Cascade II EMCCD camera controlled by Metamorph software (Molecular Devices).

The cotransfection efficiency of the human TUBB3-V5- and the Drosophila eGFP-SKL-containing plasmids, and the incorporation of wildtype or mutant Tubb3 into cellular microtubules were verified by immunostaining. After 30 min on ConA-treated coverslips, the transfected cells were fixed in -20°C methanol for 10 min, blocked in 1% bovine serum albumin, 0.1% Triton X-100 in phosphate-buffered saline (PBS) for 30 min, then incubated with mouse anti-V5 antibody (46-0705, Invitrogen) and rabbit anti-GFP antibody (Y414554, ABM) at 1:5000 and 1:1000, respectively, for 2 h at room temperature, washed with PBS, treated with Alexa-555-labeled-antimouse (A-21422, Invitrogen) and Alexa-633-labeled-antirabbit (A-21070, Invitrogen) secondary antibodies at 1:500 for 1 h at room temperature, washed with PBS then incubated with FITC-conjugated monoclonal anti-α-tubulin antibody DM1A (F2168, Sigma), and finally washed again with PBS before being mounted in ProLong anti-fade media (P36982, Invitrogen) and imaged with a Leica TCS SP2 scanning confocal microscope with a 63 × 1.40 N.A. oil objective using Las\_AF Leica confocal software. Cotransfection was scored as the number of GFP-SKL positive cells that were also positive for Tubb3-V5, either wildtype or mutant, and was >80%. Total tubulin levels were determined by quantifying anti-α-tubulin DM1A signal in cells fixed without prior extraction of soluble tubulin, and was 3-7% higher in cells transfected with mutant or wildtype TUBB3-V5 plasmids, relative to their nontransfected neighbors (anti-V5 positive and negative cells, respectively).

### Analysis of S2 cell transport assay

Cytochalasin D-treated S2 cells plated on ConA-coated slides form long, thin projections, of which those  $\leq 1~\mu m$  wide house microtubules that are >90% oriented with their plus-ends towards the projection tips and minus-ends towards the cell body (Kural *et al.*, 2005; Ally *et al.*, 2009; Lu *et al.*, 2013; Winding *et al.*, 2016). Projections  $< \sim 1~\mu m$  wide were selected for analysis, which were of similar lengths in cells transfected with wildtype, R380C, or D417H tubulin

(Supplemental Figure S4). KymoAnalyzer was used to analyze movements by tracing from the base of each projection to its tip with the polyline tool to generate kymographs (Neumann et al., 2017). The kymographs were then blinded and in each kymograph, the trajectory of each peroxisome was manually traced with the polyline tool. Plus-end directed run length for peroxisomes was defined as the distance of continuous movement > 350 nm at constant velocity toward the projection tip. Time in motion was calculated as the cumulative time each peroxisome was undergoing unidirectional movement. Time paused was defined as the percent time peroxisomes that displayed at least one continuous unidirectional movement were not in motion. Peroxisomes that displayed no directed movements during the duration of the time-lapse were classified as nonmotile and, as such, were not considered paused and were excluded from other calculations. Pause frequency was determined as the rate at which motile peroxisomes stopped moving and entered the paused state. The frequency of switch is the rate at which a motile peroxisome that has traveled > 350 nm at constant velocity in one direction then travels > 350 nm at constant velocity in the opposite direction.

# MD simulations and elastic network modeling

Structures for yeast tubulin within a microtubule polymerized using GTP (PDB ID: 5W3F) and human kinesin-1 KIF5B (PDB ID:3J8Y) were obtained from the protein data bank (PDB; Berman et al., 2000). For detailed information see Supplemental Material. Briefly, the tubulin R380C mutation was introduced using PyMOL (Schrodinger). Wildtype and R380C tubulin structures were relaxed via two independent MD simulations for each using GROMACS (Pronk et al., 2013). Kinesin was docked to the four relaxed tubulin structures using HADDOCK and for each, a single lowest energy structure of the bottom intermolecular energy cluster was selected for analysis (Dominguez et al., 2003; Vries et al., 2010). Each of the docked structures was relaxed to remove inappropriate contacts using two independent MD simulations, resulting in four wildtype tubulin-kinesin, and four R380C tubulin-kinesin structures. The RMSF for each structure were computed using the rms tool in GROMACS, and used to determine the quadratic mean RMSF for wildtype and R380C complexes (Kuzmanic and Zagrovic, 2010).

The relaxed structures of wildtype and R380C tubulin were assembled to construct a five heterodimer long, 13 protofilament microtubule segment using Chimera (Pettersen et al., 2004). A central heterodimer was then replaced with the respective kinesin-bound tubulin-GDP structure determined above. All-atom structures of the kinesin bound to wildtype and R380C microtubules were used to estimate kinesin motion dynamics using nonlinear rigid block normal-mode modeling (NOLB; Hoffmann and Grudinin, 2017). Linear changes in normal modes of motion were determined by calculating the pseudo eigenvectors between the center of mass of the initial and final conformation states across the mode. Changes in motion direction were determined by defining a linear pseudo eigenvector for each atom across the curvilinear path of kinesin motion using 0.05 motion amplitude. Reference vectors were defined as connecting the all-atom centroid coordinates of two longitudinal tubulin dimers in the kinesin-bound protofilament, or the alphacarbon coordinates of kinesin residues 246 and 270 at the ends of helix  $\alpha 4$ . Percent overlap measures the difference between the pseudo eigenvector and reference vector.

### Statistical analysis and reproducibility

Statistical analyses were carried out using Prism7 (GraphPad) or R statistical software (R-Core-Team, 2020). The unpaired Student's t test was used to analyze data from the peroxisome transport assays. The Kolmogorov-Smirnov test was used to assess statistical significance of run length data that did not fit a normal distribution. Microtubule length distributions in TIRF microscopy assays were compared using the unpaired t test. The relevant statistical tests, p values, sample sizes, number of trials, SEM (standard error of mean), and SD are indicated in the corresponding figure legends. \*  $p \le$ 0.05, \*\*  $p \le 0.01$ , \*\*\*  $p \le 0.001$ , ns = not statistically significant.

### **ACKNOWLEDGMENTS**

We thank Anyuta Gelfand and Kari Barlan for help with S2 cells experiments, J. Moore for tips on protein purification, and E. Engle and G. Goshima for useful reagents. This work was supported by National Science Foundation (NSF) grant number MCB-1846262 to M.L.G., NSF grant ABI-1661391 and National Institutes of Health (NIH) grants R01GM127701 and R01HG012117 to R.L.J., NIH grant R35GM131752 to V.I.G., and NIH grant R01GM143302 to I.C.S.

#### **REFERENCES**

- Al-Haddad C, Boustany R-M, Rachid E, Ismail K, Barry B, Chan W-M, Engle E (2020). KIF21A pathogenic variants cause congenital fibrosis of extraocular muscles type 3. Ophthalmic Genet 42, 1-5.
- Ally S, Larson AG, Barlan K, Rice SE, Gelfand VI (2009). Opposite-polarity motors activate one another to trigger cargo transport in live cells. J Cell Biol 187, 1071-1082.
- Asselin L, Alvarez JR, Heide S, Bonnet CS, Tilly P, Vitet H, Weber C, Bacino CA, Baranaño K, Chassevent A, et al. (2020). Mutations in the KIF21B kinesin gene cause neurodevelopmental disorders through imbalanced canonical motor activity. Nat Commun 11, 2441.
- Atherton J, Farabella I, Yu I-M, Rosenfeld SS, Houdusse A, Topf M, Moores CA (2014). Conserved mechanisms of microtubule-stimulated ADP release, ATP binding, and force generation in transport kinesins. eLife 3, e03680.
- Bahi-Buisson N, Poirier K, Fourniol F, Saillour Y, Valence S, Lebrun N, Hully M, Bianco CF, Boddaert N, Elie C, et al. (2014). The wide spectrum of tubulinopathies: what are the key features for the diagnosis? Brain 137, 1676-1700.
- Balasubramanian R, Chew S, MacKinnon SE, Kang PB, Andrews C, Chan W-M, Engle EC (2015). Expanding the Phenotypic Spectrum and Variability of Endocrine Abnormalities Associated With TUBB3 E410K Syndrome. J Clin Endocrinol Metabolism 100, E473-E477.
- Barlan K, Gelfand VI (2017). Microtubule-Based Transport and the Distribution, Tethering, and Organization of Organelles. Csh Perspect Biol 9,
- Baron DM, Fenton AR, Saez-Atienzar S, Giampetruzzi A, Sreeram A, Shankaracharya, Keagle PJ, Doocy VR, Smith NJ, Danielson EW, et al. (2022). ALS-associated KIF5A mutations abolish autoinhibition resulting in a toxic gain of function. Cell Reports 39, 110598.
- Benoit M, Asenjo AB, Paydar M, Dhakal S, Kwok BH, Sosa H (2021). Structural basis of mechano-chemical coupling by the mitotic kinesin KIF14. Nat Commun 12, 3637.
- Benoit M, Hunter B, Allingham JS, Sosa H (2023). New insights into the mechanochemical coupling mechanism of kinesin-microtubule complexes from their high-resolution structures. Biochem Soc Trans 51,
- Berman HM, Westbrook J, Feng Z, Gilliland G, Bhat TN, Weissig H, Shindyalov IN, Bourne PE (2000). The Protein Data Bank. Nucleic Acids Res 28, 235-242.
- Bianchi S, Riel WE van, Kraatz SHW, Olieric N, Frey D, Katrukha EA, Jaussi R, Missimer J, Grigoriev I, Olieric V, et al. (2016). Structural basis for misregulation of kinesin KIF21A autoinhibition by CFEOM1 disease mutations. Sci Rep 6, 30668.
- Case RB, Pierce DW, Hom-Booher N, Hart CL, Vale RD (1997). The directional preference of kinesin motors is specified by an element outside of the motor catalytic domain. Cell 90, 959-966.
- Cederquist GY, Luchniak A, Tischfield MA, Peeva M, Song Y, Menezes MP, Chan W-M, Andrews C, Chew S, Jamieson RV, et al. (2012). An inherited TUBB2B mutation alters a kinesin-binding site and causes polymicrogyria, CFEOM and axon dysinnervation. Hum Mol Genet 21, 5484-5499.
- Cheng L, Desai J, Miranda CJ, Duncan JS, Qiu W, Nugent AA, Kolpak AL, Wu CC, Drokhlyansky E, Delisle MM, et al. (2014). Human CFEOM1 Mutations Attenuate KIF21A Autoinhibition and Cause Oculomotor Axon Stalling. Neuron 82, 334–349.

- Cheon CK, Lim S-H, Kim Y-M, Kim D, Lee N-Y, Yoon T-S, Kim N-S, Kim E, Lee J-R (2017). Autosomal dominant transmission of complicated hereditary spastic paraplegia due to a dominant negative mutation of KIF1A, SPG30 gene. Sci Rep 7, 12527.
- Chew S, Balasubramanian R, Chan W-M, Kang PB, Andrews C, Webb BD, Mackinnon SE, Oystreck DT, Rankin J, Crawford TO, et al. (2013). A novel syndrome caused by the E410K amino acid substitution in the neuronal  $\beta$ -tubulin isotype 3. Brain 136, 522–535.
- Chiba K, Takahashi H, Chen M, Obinata H, Arai S, Hashimoto K, Oda T, McKenney RJ, Niwa S (2019). Disease-associated mutations hyperactivate KIF1A motility and anterograde axonal transport of synaptic vesicle precursors. Proc Natl Acad Sci USA 24, 201905690.
- Cook AD, Manka SW, Wang S, Moores CA, Atherton J (2020). A microtubule RELION-based pipeline for cryo-EM image processing. J Struct Biol 209, 107402.
- Coy DL, Hancock WO, Wagenbach M, Howard J (1999). Kinesin's tail domain is an inhibitory regulator of the motor domain. Nat Cell Biol 1, 288–292.
- Cushion TD, Dobyns WB, Mullins JGL, Stoodley N, Chung S-K, Fry AE, Hehr U, Gunny R, Aylsworth AS, Prabhakar P, et al. (2013). Overlapping cortical malformations and mutations in TUBB2B and TUBA1A. Brain: A Journal of Neurology 136, 536–548.
- Cushion TD, Leca I, Keays DA (2023). MAPping tubulin mutations. Front Cell Dev Biol 11, 1136699.
- Dominguez C, Boelens R, Bonvin A (2003). HADDOCK: A Protein–Protein Docking Approach Based on Biochemical or Biophysical Information. J Am Chem Soc 125, 1731–1737.
- Fourniol F, Moores CA (2010). Kinesin motor activation: Microtubules pull the switches. Proc Natl Acad Sci USA 107, 3949–3950.
- Friedman DS, Vale RD (1999). Single-molecule analysis of kinesin motility reveals regulation by the cargo-binding tail domain. Nat Cell Biol 1, 293–297.
- Gabrych DR, Lau VZ, Niwa S, Silverman MA (2019). Going Too Far Is the Same as Falling Short: Kinesin-3 Family Members in Hereditary Spastic Paraplegia. Front Cell Neurosci 13, 419.
- Gigant B, Wang W, Dreier B, Jiang Q, Pecqueur L, Plückthun A, Wang C, Knossow M (2013). Structure of a kinesin–tubulin complex and implications for kinesin motility. Nat Struct Mol Biol 20, 1001–1007.
- Gilbert SP, Guzik-Lendrum S, Rayment I (2018). Kinesin-2 motors: Kinetics and biophysics. J Biol Chem 293, 4510–4518.
- Guillaud L, El-Agamy SE, Otsuki M, Terenzio M (2020). Anterograde Axonal Transport in Neuronal Homeostasis and Disease. Front Mol Neurosci 13, 556175
- Hancock WO (2016). The Kinesin-1 Chemomechanical Cycle: Stepping Toward a Consensus. Biophys J 110, 1216–1225.
- Hoff KJ, Neumann AJ, Moore JK (2022). The molecular biology of tubulinopathies: Understanding the impact of variants on tubulin structure and microtubule regulation. Front Cell Neurosci 16, 1023267.
- Hoffmann A, Grudinin S (2017). NOLB: Nonlinear Rigid Block Normal-Mode Analysis Method. J Chem Theory Comput 13, 2123–2134.
- Howes SC, Geyer EA, LaFrance B, Zhang R, Kellogg EH, Westermann S, Rice LM, Nogales E (2017). Structural differences between yeast and mammalian microtubules revealed by cryo-EM. J Cell Biol 216, 2669–2677.
- Johnson V, Ayaz P, Huddleston P, Rice LM (2011). Design, Overexpression, and Purification of Polymerization-Blocked Yeast  $\alpha\beta$ -Tubulin Mutants. Biochemistry 50, 8636–8644.
- Jurgens JA, Barry BJ, Lemire G, Chan W-M, Whitman MC, Shaaban S, Robson CD, MacKinnon S, England EM, McMillan HJ, et al. (2021). Novel variants in TUBA1A cause congenital fibrosis of the extraocular muscles with or without malformations of cortical brain development. Eur J Hum Genet 29, 816–826.
- Kalantari S, Filges I (2020). 'Kinesinopathies': emerging role of the kinesin family member genes in birth defects. J Med Genet 57, 797–807.
- Kapitein LC, Hoogenraad CC (2015). Building the Neuronal Microtubule Cytoskeleton. Neuron 87, 492–506.
- Kulić IM, Brown AEX, Kim H, Kural C, Blehm B, Selvin PR, Nelson PC, Gelfand VI (2008). The role of microtubule movement in bidirectional organelle transport. Proc National Acad Sci 105, 10011–10016.
- Kural C, Kim H, Syed S, Goshima G, Gelfand VI, Selvin PR (2005). Kinesin and dynein move a peroxisome in vivo: a tug-of-war or coordinated movement? Science 308, 1469–1472.
- Kuzmanic A, Zagrovic B (2010). Determination of Ensemble-Average Pairwise Root Mean-Square Deviation from Experimental B-Factors. Biophys J 98, 861–871.

- Lee J, Srour M, Kim D, Hamdan FF, Lim S-H, Brunel-Guitton C, Décarie J-C, Rossignol E, Mitchell GA, Schreiber A, et al. (2015). De Novo Mutations in the Motor Domain of KIF1A Cause Cognitive Impairment, Spastic Paraparesis, Axonal Neuropathy, and Cerebellar Atrophy. Hum Mutat 36, 69–78.
- Lu W, Castillo U, Gelfand VI (2013). Organelle Transport in Cultured Drosophila Cells: S2 Cell Line and Primary Neurons. J Vis Exp, e50838.
- MacKinnon S, Oystreck DT, Andrews C, Chan W-M, Hunter DG, Engle EC (2014). Diagnostic Distinctions and Genetic Analysis of Patients Diagnosed with Moebius Syndrome. Ophthalmology 121, 1461–1468.
- Marzo MG, Griswold JM, Ruff KM, Buchmeier RE, Fees CP, Markus SM (2019). Molecular basis for dyneinopathies reveals insight into dynein regulation and dysfunction. Elife 8, e47246.
- Minoura I, Takazaki H, Ayukawa R, Saruta C, Hachikubo Y, Uchimura S, Hida T, Kamiguchi H, Shimogori T, Muto E (2016). Reversal of axonal growth defects in an extraocular fibrosis model by engineering the kinesinmicrotubule interface. Nat Commun 7, 10058.
- Mogre SS, Brown AI, Koslover EF (2020). Getting around the cell: physical transport in the intracellular world. Phys Biol 17, 061003.
- Muto E, Sakai H, Kaseda K (2005). Long-range cooperative binding of kinesin to a microtubule in the presence of ATP. J Cell Biol 168, 691–696.
- Nakata T, Hirokawa N (2003). Microtubules provide directional cues for polarized axonal transport through interaction with kinesin motor head. J Cell Biol 162, 1045–1055.
- Nakata T, Niwa S, Okada Y, Perez F, Hirokawa N (2011). Preferential binding of a kinesin-1 motor to GTP-tubulin-rich microtubules underlies polarized vesicle transport. J Cell Biol 194, 245–255.
- Neumann S, Chassefeyre R, Campbell GE, Encalada SE (2017). KymoAnalyzer: a software tool for the quantitative analysis of intracellular transport in neurons. Traffic (Copenhagen, Denmark) 18, 71–88.
- Nieh SE, Madou MRZ, Sirajuddin M, Fregeau B, McKnight D, Lexa K, Strober J, Spaeth C, Hallinan BE, Smaoui N, et al. (2015). De novo mutations in KIF1A cause progressive encephalopathy and brain atrophy. Ann Clin Transl Neur 2, 623–635.
- Niwa S, Takahashi H, Hirokawa N (2013). β-Tubulin mutations that cause severe neuropathies disrupt axonal transport. EMBO J 32, 1352–1364.
- Nogales E (2000). Structural insights into microtubule function. Annu Rev Biochem 69, 277–302.
- Nsamba ET, Bera A, Costanzo M, Boone C, Gupta ML (2021). Tubulin isotypes optimize distinct spindle positioning mechanisms during yeast mitosis. J Cell Biol 220, e202010155.
- Peet DR, Burroughs NJ, Cross RA (2018). Kinesin expands and stabilizes the GDP-microtubule lattice. Nat Nanotechnol 13, 386–391.
- Pettersen EF, Goddard TD, Huang CC, Couch GS, Greenblatt DM, Meng EC, Ferrin TE (2004). UCSF Chimera—A visualization system for exploratory research and analysis. J Comput Chem 25, 1605–1612.
- Pronk S, Páll S, Schulz R, Larsson P, Bjelkmar P, Apostolov R, Shirts MR, Smith JC, Kasson PM, Spoel D van der, et al. (2013). GROMACS 4.5: A high-throughput and highly parallel open source molecular simulation toolkit. Bioinformatics 29, 845–854.
- R-Core-Team (2020). R: A Language and Environment for Statistical Computing. Vienna, Austria: R Foundation for Statistical Computing, www.R-project.org/ (accessed 2 June 2022).
- Reed NA, Cai D, Blasius TL, Jih GT, Meyhofer E, Gaertig J, Verhey KJ (2006). Microtubule Acetylation Promotes Kinesin-1 Binding and Transport. Curr Biol 16, 2166–2172.
- Rice S, Cui Y, Sindelar C, Naber N, Matuska M, Vale R, Cooke R (2003). Thermodynamic Properties of the Kinesin Neck-Region Docking to the Catalytic Core. Biophys J 84, 1844–1854.
- Rice S, Lin AW, Safer D, Hart CL, Naber N, Carragher BO, Cain SM, Pechatnikova E, Wilson-Kubalek EM, Whittaker M, et al. (1999). A structural change in the kinesin motor protein that drives motility. Nature 402, 778–784.
- Ryan MM, Engle EC (2015). Neuromuscular Disorders of Infancy, Childhood, and Adolescence (2nd edition). Part Vii Special Clin Problems, 922–957.
- Schneider CA, Rasband WS, Eliceiri KW (2012). NIH Image to ImageJ: 25 years of image analysis. Nat Methods 9, 671–675.
- Shang Z, Zhou K, Xu C, Csencsits R, Cochran JC, Sindelar CV (2014). High-resolution structures of kinesin on microtubules provide a basis for nucleotide-gated force-generation. eLife 3, e04686.
- Shima T, Morikawa M, Kaneshiro J, Kambara T, Kamimura S, Yagi T, Iwamoto H, Uemura S, Shigematsu H, Shirouzu M, et al. (2018). Kinesin-bindingtriggered conformation switching of microtubules contributes to polarized transport. J Cell Biol 217, 4164–4183.
- Sindelar CV, Downing KH (2010). An atomic-level mechanism for activation of the kinesin molecular motors. Proc National Acad Sci USA 107, 4111–4116.

- Sirajuddin M, Rice LM, Vale RD (2014). Regulation of microtubule motors by tubulin isotypes and post-translational modifications. Nat Cell Biol 16, 335-344.
- Soustelle L, Aimond F, Andrés CL, Brugioti V, Raoul C, Layalle S (2023). ALS-associated KIF5A mutation causes locomotor deficits associated with cytoplasmic inclusions, alterations of neuromuscular junctions and motor neuron loss. J Neurosci 43, 8058-8072.
- Stock MF, Guerrero J, Cobb B, Eggers CT, Huang TG, Li X, Hackney DD (1999). Formation of the compact confomer of kinesin requires a COOH-terminal heavy chain domain and inhibits microtubule-stimulated ATPase activity. J Biol Chem 274, 14617-14623.
- Tas RP, Chazeau A, Cloin BMC, Lambers MLA, Hoogenraad CC, Kapitein LC (2017). Differentiation between Oppositely Oriented Microtubules Controls Polarized Neuronal Transport. Neuron 96, 1264-1271.e5.
- Ti S-C, Pamula MC, Howes SC, Duellberg C, Cade NI, Kleiner RE, Forth S, Surrey T, Nogales E, Kapoor TM (2016). Mutations in Human Tubulin Proximal to the Kinesin-Binding Site Alter Dynamic Instability at Microtubule Plus- and Minus-Ends. Developmental Cell 37, 72-84
- Tischfield MA, Baris HN, Wu C, Rudolph G, Maldergem LV, He W, Chan W-M, Andrews C, Demer JL, Robertson RL, et al. (2010). Human TUBB3 Mutations Perturb Microtubule Dynamics, Kinesin Interactions, and Axon Guidance. Cell 140, 74-87.
- Toprak E, Yildiz A, Hoffman MT, Rosenfeld SS, Selvin PR (2009). Why kinesin is so processive. Proc National Acad Sci USA 106, 12717-
- Traboulsi EI, Engle EC (2004). Mutations in KIF21A are responsible for CFEOM1 worldwide. Ophthalmic Genet 25, 237-239.
- Uchimura S, Oguchi Y, Hachikubo Y, Ishiwata S, Muto E (2010). Key residues on microtubule responsible for activation of kinesin ATPase. EMBO J 29, 1167-1175.
- Uchimura S, Oguchi Y, Katsuki M, Usui T, Osada H, Nikawa J, Ishiwata S, Muto E (2006). Identification of a strong binding site for kinesin on the microtubule using mutant analysis of tubulin. EMBO J 25, 5932-5941.

- Vilfan A, Frey E, Schwabl F, Thormählen M, Song Y-H, Mandelkow E (2001). Dynamics and cooperativity of microtubule decoration by the motor protein kinesin. J Mol Biol 312, 1011-1026.
- Vries SJ, Dijk M, Bonvin A (2010). The HADDOCK web server for datadriven biomolecular docking. Nat Protoc 5, 883–897.
- Whitman MC, Andrews C, Chan W-M, Tischfield MA, Stasheff SF, Brancati F, Ortiz-Gonzalez X, Nuovo S, Garaci F, Mackinnon SE, et al. (2016). Two unique TUBB3 mutations cause both CFEOM3 and malformations of cortical development. Am J Med Genet 170A, 297-305.
- Whitman MC, Jurgens JA, Hunter DG, Engle EC (2004). Congenital Fibrosis of the extraocular muscles overview. [Updated 2021 Aug 12]. In: GeneReviews® [Internet], eds. MP Adam , J Feldman , GM Mirzaa , RA Pagon , SE Wallace , LJH Bean , KW Gripp , A Amemiya , Seattle, WA: University of Washington.
- Wijeratne SS, Fiorenza SA, Neary AE, Subramanian R, Betterton MD (2022). Motor guidance by long-range communication on the microtubule highway. Proc National Acad Sci 119, e2120193119
- Winding M, Kelliher MT, Lu W, Wildonger J, Gelfand VI (2016). Role of kinesin-1-based microtubule sliding in Drosophila nervous system development. Proc National Acad Sci 113, E4985-E4994.
- Yajima J, Cross RA (2005). A torque component in the kinesin-1 power stroke. Nat Chem Biol 1, 338-341.
- Yamada K, Andrews C, Chan W-M, McKeown CA, Magli A, Berardinis de T, Loewenstein A, Lazar M, O'Keefe M, Letson R, et al. (2003). Heterozygous mutations of the kinesin KIF21A in congenital fibrosis of the extraocular muscles type 1 (CFEOM1). Nat Genet 35, 318-321.
- Yamada K, Chan W-M, Andrews C, Bosley TM, Sener EC, Zwaan JT, Mullaney PB, Öztürk BT, Akarsu AN, Sabol LJ, et al. (2004). Identification of KIF21A Mutations as a Rare Cause of Congenital Fibrosis of the Extraocular Muscles Type 3 (CFEOM3). Invest Ophth Vis Sci 45, 2218–2223.
- Zhao C, Takita J, Tanaka Y, Setou M, Nakagawa T, Takeda S, Yang HW, Terada S, Nakata T, Takei Y, et al. (2001). Charcot-Marie-Tooth disease type 2A caused by mutation in a microtubule motor KIF1Bbeta. Cell 105, 587-597.